A force-based coupling scheme for peridynamics and classical elasticity

Pablo Seleson [a], Samir Beneddine [b], Serge Prudhomme [a],*

[a] Institute for Computational Engineering and Sciences, The University of Texas at Austin, 201 East 24th St. Stop C0200, Austin, TX 78712-1229, USA
[b] Department of Mechanical Engineering, École Normale Supérieure de Cachan, 61, Avenue du Président Wilson, 94235 Cachan cedex, France

ARTICLE INFO

ABSTRACT

In this work, we present a novel methodology to derive blending schemes to concurrently couple local and nonlocal models obtained from a single reference framework based upon the peridynamic theory of solid mechanics. A consistent force-based blended model that couples peridynamics and classical elasticity is presented using nonlocal weights composed of integrals of blending functions. The proposed blended model possesses desired properties of multiscale material models such as satisfying Newton's third law and passing the patch test. This approach finds useful applications in material failure for which the peridynamics theory can be used to describe regions where fracture is expected, whereas classical elasticity could be efficiently used elsewhere. Numerical experiments demonstrating the accuracy and efficiency of the blended model are presented as well as qualitative studies of the error sensitivity on different model and problem parameters. We also generalize this approach to the coupling of peridynamics and higher-order gradient models of any order.

1. Introduction

Multiscale modeling in materials science has been recognized in recent years as an important research field critical to achieving feasible and accurate descriptions of the behavior of many complex systems. Methods attempting to couple nonlocal and local models, particularly, atomistic and continuum ones, including the Quasicontinuum method [21,36,41] and the Arlequin aproach [5,6,8,9], among others, are provided in the literature; for a benchmark study of different atomistic-to-continuum coupling methods the reader is referred to [28].

An alternative approach to include fine-scale effects into classical continuum models has been taken by developing nonlocal continuum models; some of these nonlocal formulations appear in, e.g., [23–25,30] and the references cited therein. A nonlocal continuum mechanics framework, developed for the study of material failure was formulated under the peridynamics theory [37,39], by replacing the divergence of the stress tensor appearing in the Cauchy's first equation of motion in classical elasticity with an integral over a kernel based upon differences of the displacement field and not on its derivatives. Peridynamics has been applied in recent years to a wide range of applications, including deformation and damage [38], crack propagation and crack branching [18], viscoplasticity [17], polycrystal fracture [2], wave propagation [35], etc.

In this paper, we are interested in studying peridynamics as a multiscale material framework. This is motivated by the fact that peridynamics possesses a length scale, its interaction range, and thus relations between the model and system length scales may determine the behavior of the model. As a consequence, blended schemes allowing to couple models characterized by different length scales may be derived from a framework such as peridynamics. The main result of this paper involves the derivation of a blended model to couple peridynamics and classical elasticity that avoids common undesired spurious effects appearing in most multiscale material models to date.

This paper is organized as follows. In Section 2, we provide a brief description of the peridynamics and classical elasticity theories. Then, in Section 3, we describe some issues appearing in atomistic-to-continuum coupling methods; we present an example of an *ad hoc* force-based blending scheme between peridynamics and classical elasticity in Section 3.1 to motivate our methodology, and derive a consistent blended model in Section 3.2. In Section 3.3, we present discretizations of our blended model, providing insights for atomistic-to-continuum coupling approaches. A description of different blending functions and a study of nonlocal weights appearing in the blended model are presented in Section 4. Numerical results for patch test problems and point loads comparing peridynamics, classical elasticity, and the blended model are given in Section 5; we perform numerical studies of the error dependence on different model components and the model speedup. A generalized blending approach to couple peridynamics and higher-order gradient models is presented in Section 6. We conclude with a summary and future plans in Section 7.

* Corresponding author. Tel.: +1 512 475 8629; fax: +1 512 471 8694.
E-mail addresses: seleson@ices.utexas.edu (P. Seleson), sbeneddi@ens-cachan.fr (S. Beneddine), serge@ices.utexas.edu (S. Prudhomme).

2. The peridynamics theory

Peridynamics (PD) is a nonlocal reformulation of classical continuum mechanics proposed in [37]. One of the major features of this theory is the absence of spatial derivatives of displacement fields, allowing it to be implemented for the description of material failure [18,38]. The original PD theory was based upon pairwise interactions providing Poisson's ratios of $v = 1/4$ (in 3D); it was named *bond-based* PD theory. This formulation was later generalized to multibody interactions under the *state-based* PD theory [39], allowing for general Poisson's ratios. Relations between state-based and bond-based PD constitutive models are provided in [33,34]. In the present paper we restrict ourselves to bond-based peridynamic models.

The peridynamic equation of motion for a point $\mathbf{x}$ in a body $\Omega \in \mathbb{R}^d, d = 1, 2,$ or 3, is

$$\rho(\mathbf{x})\ddot{\mathbf{u}}(\mathbf{x}, t) = \int_{\mathscr{H}_{\mathbf{x}}} \mathbf{f}(\mathbf{u}(\mathbf{x}', t) - \mathbf{u}(\mathbf{x}, t), \mathbf{x}' - \mathbf{x})dV_{\mathbf{x}'} + \mathbf{b}(\mathbf{x}, t), \qquad (1)$$

for $t \geqslant 0$ with ρ the mass density, $\mathbf{u}$ the displacement field, $\mathbf{b}$ the body force density, and $\mathbf{f}$ the pairwise force function with units of force per volume squared. In PD, the dynamics of a point $\mathbf{x} \in \Omega$ is determined by its interactions with all surrounding points $\mathbf{x}'$ within the *neighborhood*

$$\mathscr{H}_{\mathbf{x}} := \{\mathbf{x}' \in \mathbb{R}^d : \|\mathbf{x}' - \mathbf{x}\| \leqslant \varepsilon\}, \qquad (2)$$

where the radius ε is called the *horizon* of the PD model. In order to preserve linear and angular momenta, the pairwise force function has to satisfy the following two conditions:

$$\mathbf{f}(-\boldsymbol{\eta}, -\boldsymbol{\xi}) = -\mathbf{f}(\boldsymbol{\eta}, \boldsymbol{\xi}) \quad \forall \boldsymbol{\eta}, \boldsymbol{\xi} \in \mathbb{R}^d, \qquad (3)$$

$$(\boldsymbol{\xi} + \boldsymbol{\eta}) \times \mathbf{f}(\boldsymbol{\eta}, \boldsymbol{\xi}) = \mathbf{0} \quad \forall \boldsymbol{\eta}, \boldsymbol{\xi} \in \mathbb{R}^d, \qquad (4)$$

which are referred to as the *linear admissibility condition* and *angular admissibility condition*, respectively. The vector $\boldsymbol{\xi} := \mathbf{x}' - \mathbf{x}$ represents the reference relative position between the points $\mathbf{x}'$ and $\mathbf{x}$, and $\boldsymbol{\eta} := \mathbf{u}(\mathbf{x}', t) - \mathbf{u}(\mathbf{x}, t)$ represents their relative displacement; furthermore, $\boldsymbol{\xi} + \boldsymbol{\eta}$ is the current relative position between the two points. For additional details on general properties of bond-based PD models, the reader is referred to [37].

We now show that the linear admissibility condition (3) can be connected to the classical Newton's third law, i.e., given two objects A and B, if object A exerts a force $\mathbf{F}$ on object B then object B exerts a force of equal magnitude and opposite direction $-\mathbf{F}$ on object A. For that purpose, we take a look at the interaction between two arbitrary material regions Ω_A and Ω_B inside a given body Ω and compute the forces that each material region exerts on the other one. The force that Ω_B exerts on Ω_A is computed as

$$\mathbf{F}_{BA} = \int_{\Omega_A} \int_{\Omega_B} \chi_\varepsilon(\|\boldsymbol{\xi}\|)\mathbf{f}(\boldsymbol{\eta}, \boldsymbol{\xi})dV_{\mathbf{x}'}dV_{\mathbf{x}},$$

whereas the force that Ω_A exerts on Ω_B is

$$\mathbf{F}_{AB} = \int_{\Omega_B} \int_{\Omega_A} \chi_\varepsilon(\|\boldsymbol{\xi}\|)\mathbf{f}(\boldsymbol{\eta}, \boldsymbol{\xi})dV_{\mathbf{x}'}dV_{\mathbf{x}},$$

where χ_ε is the characteristic function

$$\chi_\varepsilon(\|\boldsymbol{\xi}\|) := \begin{cases} 1 & \|\boldsymbol{\xi}\| \leqslant \varepsilon, \\ 0 & \text{otherwise}. \end{cases}$$

Thanks to the antisymmetry property of the pairwise force function (3), it is easy to conclude that $\mathbf{F}_{AB} = -\mathbf{F}_{BA}$. As a consequence, the nonlocal interaction between two finite-sized material regions satisfy Newton's third law whenever the PD pairwise force function satisfies the linear admissibility condition (3).

The horizon ε represents a length scale in the PD theory. Therefore, PD is suitable for multiscale modeling [1,2,11,19,26,31]. Concurrent coupling methods between PD and classical local models have appeared in the literature as follows. In [20,27], a coupling between the discretized PD and the standard finite element method is presented; our goal however is to achieve a *continuum formulation* for the coupled system. An approach to couple nonlocal and local continuum models through PD appears in [19,26], where an energy-based blending of PD and classical elasticity (CE) through the Arlequin method is presented; in contrast to this work, we derive here a coupling scheme starting from *a single framework*, and obtain a blended model at the level of the equations of motion, avoiding common undesired spurious effects. An example of the multiscale aspects of PD appears in [40], where PD is shown to converge to CE in the limit of $\varepsilon \to 0$. The Cauchy's first equation of motion in CE is

$$\rho(\mathbf{x})\ddot{\mathbf{u}}(\mathbf{x}, t) = \nabla \cdot \boldsymbol{\sigma}(\mathbf{x}, t) + \mathbf{b}(\mathbf{x}, t), \qquad (5)$$

where $\boldsymbol{\sigma}$ represents the first Piola–Kirchhoff stress tensor. A major difference between the nonlocal PD and the local CE theories is that in PD a direct interaction between points separated by a finite distance is assumed; in contrast, in CE the value of the stress tensor at a given point usually depends on the value of $\nabla \mathbf{u}$ only at that point. In [40], it is shown that under appropriate differentiability assumptions, (1) can be expressed in the form (5) by replacing $\boldsymbol{\sigma}$ with a *nonlocal* stress tensor.

3. One-dimensional force-based blending of linear peridynamics and classical elasticity

Methods have been proposed in the past for concurrent multiscale modeling in an attempt to couple local and nonlocal models. These approaches are summarized, for example, in [14] in the case of atomistic-to-continuum (AtC) coupling methods. A special class of methods, in which atomistic and continuum models are coupled together by means of an overlapping or bridging domain, appear under the so-called *blending methods* [3,4,13,16], *bridging domain methods* [7,32,42], or *Arlequin method* [5,8,9,29], among others. Most of these approaches can be considered as either *force-based* AtC coupling methods, based upon equilibrating internal and external forces at each point using blended equations of motion [3,4,16] or *energy-based* AtC coupling methods, based upon minimization of energy partitions under given constraints [5,7–9,29,32,42].

A major issue of AtC coupling schemes is due to the combination of two mathematically distinct descriptions of the same material. The differences in nature between these two models are twofold. First, atomistic models are based on discrete descriptions, in contrast to continuum models; as a consequence, a blended scheme would involve discrete and continuum terms. Second, atomistic models are usually nonlocal, whereas classical continuum models are local; therefore, potential lack of reciprocity in the interaction between points in the system may exist, leading for example to the appearance of so-called *ghost-forces* or possibly to the fact that *Newton's third law* fails to hold. These drawbacks may be avoided by deriving a blending scheme from a nonlocal continuum framework, as it is demonstrated in Section 3.2.

In this work, we will only be concerned with linear one-dimensional PD models. The models we attempt to blend are:

1. *Peridynamics:* The one-dimensional linear PD equation of motion is

$$\rho(x)\frac{\partial^2 u}{\partial t^2}(x, t) = \int_{x-\varepsilon}^{x+\varepsilon} C(|x' - x|)(u(x', t) - u(x, t))dx' + b(x, t),$$

$$(6)$$

assuming a pairwise equilibrated reference configuration [37], with $C(|x'-x|)$ the micromodulus satisfying

$$\frac{1}{2}\int_{-\varepsilon}^{\varepsilon}C(|\xi|)\xi^2 d\xi =: K < \infty. \tag{7}$$

2. *Classical elasticity*: The corresponding CE model, to which (6) converges to, in the limit of $\varepsilon \to 0$ [35], is

$$\rho(x)\frac{\partial^2 u}{\partial t^2}(x,t) = K\frac{\partial^2 u}{\partial x^2}(x,t) + b(x,t), \tag{8}$$

i.e., the one-dimensional wave equation.

3.1. An example of classical force-based blending

To illustrate how classical force-based blending methods work, we present, as an example, an *external blending* (cf. [13, type III method]) between models (6) and (8). Following standard implementations of blending methods, the domain of interest Ω is divided into three non-overlapping subdomains:

– Ω_{PD}: Domain described by the PD model;
– Ω_{CE}: Domain described by the CE model;
– Ω_b: Bridging domain where both PD and CE models coexist,

with $\overline{\Omega} = \overline{\Omega_{PD} \cup \Omega_b \cup \Omega_{CE}}$. The domain Ω_{PD} usually contains regions where discontinuities are present or may be generated, and thus the nonlocal model should be used there. In contrast, Ω_{CE} should contain regions away from discontinuities and, as a consequence, the local model can be used. The main question is how to blend the PD and CE equations in a single expression and, in particular, how the coupling is achieved in Ω_b.

We introduce a blending function $\beta(x)$ such that

$$\beta(x) = \begin{cases} 1, & \text{in } \Omega_{PD}, \\ \in (0,1), & \text{in } \Omega_b, \\ 0, & \text{in } \Omega_{CE}. \end{cases} \tag{9}$$

Using this blending function, we can derive a blended PD/CE model as follows:

$$\rho(x)\frac{\partial^2 u}{\partial t^2}(x,t) = \beta(x)\int_{x-\varepsilon}^{x+\varepsilon} C(|x'-x|)(u(x',t)-u(x,t))dx'$$
$$+ (1-\beta(x))K\frac{\partial^2 u}{\partial x^2}(x,t) + b(x,t). \tag{10}$$

This model recovers (6) for $\beta \equiv 1$ and (8) for $\beta \equiv 0$, as desired.

In order to evaluate the suitability of the blended scheme (10) as multiscale material model, we need to check whether the following properties hold:

– *Newton's third law*. Newton's third law translates into the linear admissibility condition (3) for our nonlocal continuum model.
– *Patch test consistency*. We say that a method is *patch test consistent* if a linear profile is a solution to a static problem with no external loads [22].

To check patch test consistency, we consider a static problem with no external loads. Then, (10) can be written as

$$\beta(x)\int_{x-\varepsilon}^{x+\varepsilon} C(|x'-x|)(u(x')-u(x))dx' + (1-\beta(x))K\frac{\partial^2 u}{\partial x^2}(x) = 0.$$

Let a linear deformation be $u(x) = Fx + u_0$ with F and u_0 constant; thus $u(x')-u(x) = F(x'-x)$ and $\frac{\partial^2 u}{\partial x^2} = 0$. Therefore, we get

$$\beta(x)\int_{x-\varepsilon}^{x+\varepsilon} C(|x'-x|)F(x'-x)dx' = \beta(x)F\int_{-\varepsilon}^{\varepsilon} C(|\xi|)\xi\, d\xi = 0,$$

since the integrand $C(|\xi|)\xi$ is necessarily odd. We conclude that this method is patch test consistent. In order to check whether this method satisfies the linear admissibility condition (3), we take a look at the nonlocal pairwise force function in (10), which can be expressed as[1]

$$\tilde{f}(x',x) = \beta(x)C(|x'-x|)(u(x',t)-u(x,t)).$$

The counter interaction, i.e., the nonlocal "force" that x exerts on x', is then

$$\tilde{f}(x,x') = \beta(x')C(|x-x'|)(u(x,t)-u(x',t))$$
$$= -\beta(x')C(|x'-x|)(u(x',t)-u(x,t)).$$

As a consequence, if $\beta(x) \neq \beta(x')$ we obtain

$$\tilde{f}(x',x) \neq -\tilde{f}(x,x'),$$

so that, in general, this method does not satisfy the linear admissibility condition (3) and thus violates Newton's third law. As illustrated here, an *ad hoc* blending between different models may lead to undesired spurious effects.

3.2. A consistent force-based blending scheme

In this section, we demonstrate that we are able to derive a consistent force-based blending scheme to couple PD and CE that does not introduce undesired spurious effects. We start by taking a peridynamic model as a valid framework in the entire domain Ω. Let Ω_{PD}^0 be the domain

$$\Omega_{PD}^0 := \{x \in \Omega_{PD} : \mathscr{H}_x \subset \Omega_{PD}\}. \tag{11}$$

Then, for any $x \notin \Omega_{PD}^0$, we assume that the approximation

$$u(x',t) - u(x,t) \approx \frac{\partial u}{\partial x}(x,t)(x'-x) + \frac{1}{2}\frac{\partial^2 u}{\partial x^2}(x,t)(x'-x)^2, \tag{12}$$

for $|x'-x| \leqslant \varepsilon$, provides accurate predictions of given quantities of interest, such as the average strain in the system, or the displacement at a particular point, etc.

With assumption (12) in mind, we now take (6) and write the first term on its right-hand side as

$$\int_{x-\varepsilon}^{x+\varepsilon} C(|x'-x|)(u(x',t)-u(x,t))dx'$$
$$= \int_{x-\varepsilon}^{x+\varepsilon}\left(\frac{\beta(x)+\beta(x')}{2}\right)C(|x'-x|)(u(x',t)-u(x,t))dx'$$
$$+ \int_{x-\varepsilon}^{x+\varepsilon}\left(1-\frac{\beta(x)+\beta(x')}{2}\right)C(|x'-x|)(u(x',t)-u(x,t))dx'. \tag{13}$$

The first term on the right-hand side of (13) provides the nonlocal component of the blended model. Notice that by introducing the blending function $\beta(x)$ in a symmetric way, we ensure that the kernel of this term satisfies the linear admissibility condition (3), leading to the satisfaction of Newton's third law. The second term on the right-hand side of (13) vanishes for $x \in \Omega_{PD}^0$ since in this case $\beta(x) = 1$ and $\beta(x') = 1$ for $x' \in \mathscr{H}_x$. As a consequence, this term only gives a nonzero contribution for $x \notin \Omega_{PD}^0$ for which the approximation (12) gives the expression

---

[1] The function $\tilde{f}(x',x)$ can be thought as the nonlocal "force" that x' exerts on x, in units of force per volume squared, in the blended model (10).

$$\int_{x-\varepsilon}^{x+\varepsilon}\left(1-\frac{\beta(x)+\beta(x')}{2}\right)C(|x'-x|)(u(x',t)-u(x,t))dx'$$

$$\approx \int_{x-\varepsilon}^{x+\varepsilon}\left(1-\frac{\beta(x)+\beta(x')}{2}\right)C(|x'-x|)$$

$$\times\left(\frac{\partial u}{\partial x}(x,t)(x'-x)+\frac{1}{2}\frac{\partial^2 u}{\partial x^2}(x,t)(x'-x)^2\right)dx'$$

$$=\left[\int_{-\varepsilon}^{\varepsilon}\left(1-\frac{\beta(x)+\beta(x+\xi)}{2}\right)C(|\xi|)\xi d\xi\right]\frac{\partial u}{\partial x}(x,t)$$

$$+\left[\int_{-\varepsilon}^{\varepsilon}\left(1-\frac{\beta(x)+\beta(x+\xi)}{2}\right)C(|\xi|)\xi^2 d\xi\right]\frac{1}{2}\frac{\partial^2 u}{\partial x^2}(x,t), \quad (14)$$

where we have used the change of variables $\xi = x' - x$.

By simple algebraic manipulations, we obtain (cf. (7))

(i) $\int_{-\varepsilon}^{\varepsilon}\left(1-\frac{\beta(x)+\beta(x+\xi)}{2}\right)C(|\xi|)\xi d\xi$

$=-\int_{0}^{\varepsilon}\left(\frac{\beta(x+\xi)-\beta(x-\xi)}{2}\right)C(|\xi|)\xi\, d\xi,$

(ii) $\int_{-\varepsilon}^{\varepsilon}\left(1-\frac{\beta(x)+\beta(x+\xi)}{2}\right)C(|\xi|)\xi^2 d\xi$

$=2K\left(1-\frac{\beta(x)}{2}\right)-\int_{0}^{\varepsilon}\frac{\beta(x+\xi)+\beta(x-\xi)}{2}C(|\xi|)\xi^2\, d\xi.$

Upon inserting (i) and (ii) into (14), we obtain the blended model

$$\rho(x)\frac{\partial^2 u}{\partial t^2}(x,t)=\int_{-\varepsilon}^{\varepsilon}\left(\frac{\beta(x)+\beta(x+\xi)}{2}\right)C(|\xi|)(u(x+\xi,t)-u(x,t))d\xi$$

$$-\frac{\partial u}{\partial x}(x,t)\left[\int_{0}^{\varepsilon}\left(\frac{\beta(x+\xi)-\beta(x-\xi)}{2}\right)C(|\xi|)\xi d\xi\right]$$

$$+\frac{\partial^2 u}{\partial x^2}(x,t)\left[K\left(1-\frac{\beta(x)}{2}\right)\right.$$

$$\left.-\frac{1}{2}\int_{0}^{\varepsilon}\frac{\beta(x+\xi)+\beta(x-\xi)}{2}C(|\xi|)\xi^2 d\xi\right]+b(x,t). \quad (15)$$

Remark 1. In contrast to standard force-based blending methods, where two different models are joined together and coupled through a blending function, our approach produces a coupled model derived from *a single framework*, by using a blending function.

Remark 2. There are two interesting properties to observe in the bended model (15). First, the blended model includes a weighted PD term, a weighted CE term, and, in addition, a coupling term described by the first partial derivative of the displacement field. Second, the blending is performed through *nonlocal weights*, composed of integrals of the blending function $\beta(x)$ defined in (9).

We now emphasize certain model properties of (15):

- Let $\beta(x)\equiv 1$: In this case, it is clear from (12) that the blended model (15) recovers the PD Eq. (6).
- Let $\beta(x)\equiv 0$: Inspection of (15) shows that the blended model recovers the CE model (8).
- Patch test consistency: Assume a static problem with no external loads. Let the displacement field be $u(x)=Fx+u_0$ with F and u_0 constant, so that $u(x+\xi)-u(x)=F\xi$, $\frac{\partial u}{\partial x}=F$ and $\frac{\partial^2 u}{\partial x^2}=0$. We can easily check that $u(x)$ satisfies (15) with $b\equiv 0$. Thus, the blended model (15) passes the patch test.
- Newton's third law: To demonstrate that (15) satisfies Newton's third law, we write it as

$$\rho(x)\frac{\partial^2 u}{\partial t^2}(x,t)=\int_{x-\varepsilon}^{x+\varepsilon}\left[\frac{\beta(x)+\beta(x')}{2}C(|x'-x|)(u(x',t)-u(x,t))\right.$$

$$+\left(1-\frac{\beta(x)+\beta(x')}{2}\right)C(|x'-x|)$$

$$\left.\times\left\{\frac{\partial u}{\partial x}(x,t)(x'-x)+\frac{1}{2}\frac{\partial^2 u}{\partial x^2}(x,t)(x'-x)^2\right\}\right]dx'+b(x,t)$$

$$(16)$$

and show that the kernel in (16) is antisymmetric, i.e., it satisfies the linear admissibility condition (3).

Case 1: let $x \in \Omega_{PD}^0$. Then, $\beta(x)=\beta(x')=1$, for $x'\in\mathcal{H}_x$, and the kernel in (16) reduces to

$$C(|x'-x|)(u(x',t)-u(x,t)),$$

which is clearly antisymmetric.

Case 2: let $x\notin\Omega_{PD}^0$. In this case, the Taylor expansion (12) holds, and the kernel in (16) is antisymmetric as long as the displacement field $u(x,t)$ is cubic within the neighborhood $\mathcal{H}_x$. In other words, we assume that the characteristic length scale of fluctuations of the global solution restricted to $\Omega\setminus\Omega_{PD}^0$ is much larger than the horizon ε, giving a *smooth enough* displacement field. To demonstrate that the linear admissibility condition (3) is satisfied for a cubic polynomial, let

$$u(x,t)=a_0(t)+a_1(t)x+a_2(t)x^2+a_3(t)x^3.$$

A direct calculation shows that, on one hand,

$$u(x',t)-u(x,t)=\left[a_3(t)((x')^2+x'x+x^2)+a_2(t)(x'+x)+a_1(t)\right](x'-x)$$

and, on the other hand,

$$\frac{\partial u}{\partial x}(x,t)(x'-x)+\frac{1}{2}\frac{\partial^2 u}{\partial x^2}(x,t)(x'-x)^2$$

$$=[3a_3(t)x'x+a_2(t)(x'+x)+a_1(t)](x'-x).$$

In this case, the kernel in (16) can be written as

$$C(|x'-x|)\left[a_3(t)\left(\frac{\beta(x)+\beta(x')}{2}(x'-x)^2+3x'x\right)+a_2(t)(x'+x)+a_1(t)\right](x'-x),$$

which is clearly antisymmetric. In the case of a quadratic global solution, i.e., $a_3(t)=0$, we get

$$u(x',t)-u(x,t)=\frac{\partial u}{\partial x}(x,t)(x'-x)+\frac{1}{2}\frac{\partial^2 u}{\partial x^2}(x,t)(x'-x)^2$$

and (16) is identical to (6), i.e., no approximation is made. For a global solution given by higher polynomials, e.g., a quartic one, the approximation (12) will not give an antisymmetric kernel in (16) and Newton's third law would be violated; however, in the case where the error introduced by (12) remains small, it should have little effects on the results. To achieve higher accuracy, higher Taylor expansions can be used, as shown in Section 6.

Remark 3. We note that the blended model (15) passes the patch test due to the presence of the coupling term

$$-\frac{\partial u}{\partial x}(x,t)\left[\int_{0}^{\varepsilon}\left(\frac{\beta(x+\xi)-\beta(x-\xi)}{2}\right)C(|\xi|)\xi d\xi\right]$$

which ensures cancelation of potential ghost forces. In addition, notice that this term vanishes wherever $\beta(x)=$ constant, i.e., this term does not have any contribution far away from Ω_b.

Remark 4. The blending function $\beta(x)$ is assumed to be regular enough so that it can be implemented in (13). However, no additional assumptions are made regarding the functional form of $\beta(x)$ in Ω_b. We will look at specific blending functions in Section 4.

Remark 5. It is interesting to observe that if we replace (13) by

$$\int_{x-\varepsilon}^{x+\varepsilon}C(|x'-x|)(u(x',t)-u(x,t))dx'$$

$$=\beta(x)\int_{x-\varepsilon}^{x+\varepsilon}C(|x'-x|)(u(x',t)-u(x,t))dx'$$

$$+(1-\beta(x))\int_{x-\varepsilon}^{x+\varepsilon}C(|x'-x|)(u(x',t)-u(x,t))dx',$$

then the derivations and assumptions leading to (15) give instead (10). Thus, model (10) can be viewed as a result of a local blending.

3.3. An atomistic-to-continuum coupling scheme based on a force-based blending of peridynamics and classical elasticity

The PD model (6) has been cast as a continualization of a non-local linear springs molecular dynamics (MD) model in [35] with the micromodulus

$$C(|x' - x|) = \frac{2K}{\varepsilon^2} \frac{1}{|x' - x|}. \tag{17}$$

In this case, the blended PD/CE model (15) can be written as

$$\rho(x)\frac{\partial^2 u}{\partial t^2}(x,t) = \int_{-\varepsilon}^{\varepsilon} \left(\frac{\beta(x) + \beta(x+\xi)}{2}\right)\frac{2K}{\varepsilon^2}\frac{1}{|\xi|}(u(x+\xi,t) - u(x,t))d\xi$$
$$- K\frac{\partial u}{\partial x}(x,t)\left[\frac{2}{\varepsilon^2}\int_0^{\varepsilon}\left(\frac{\beta(x+\xi) - \beta(x-\xi)}{2}\right)d\xi\right]$$
$$+ K\frac{\partial^2 u}{\partial x^2}(x,t)\left[1 - \frac{\beta(x)}{2} - \frac{1}{\varepsilon^2}\int_0^{\varepsilon}\frac{\beta(x+\xi) + \beta(x-\xi)}{2}\xi d\xi\right]$$
$$+ b(x,t). \tag{18}$$

We thus demonstrate the derivation of an AtC coupling scheme based upon the blended PD/CE model (18).

In order to obtain an AtC coupling scheme, we need to discretize (18). There are many ways to discretize nonlocal continuum models such as PD; see [15] for an overview. Following a similar discretization as in [35], we divide the domain Ω into $N_x - 1$ uniform intervals of size Δx, so that we obtain a uniform mesh with N_x equally-spaced nodes. We then assume each node represents a "cell" of length Δx; see Fig. 1.

Using a midpoint quadrature rule for the integrals in (18), we obtain for point i

$$\rho_i\frac{d^2 u_i}{dt^2}(t) = \sum_{\substack{j=-N\\j\neq 0}}^{N}\left(\frac{\beta_i + \beta_{i+j}}{2}\right)\frac{1}{\Delta x}\frac{2K}{N(N+1)}\frac{1}{|j\Delta x|}(u_{i+j}(t) - u_i(t))$$
$$- K\frac{1}{\Delta x}\frac{\partial u}{\partial x}(x_i,t)\left[\frac{2}{N(N+1)}\sum_{j=1}^{N}\left(\frac{\beta_{i+j} - \beta_{i-j}}{2}\right)\right]$$
$$+ K\frac{\partial^2 u}{\partial x^2}(x_i,t)\left[1 - \frac{\beta_i}{2} - \frac{1}{N(N+1)}\sum_{j=1}^{N}\frac{\beta_{i+j} + \beta_{i-j}}{2}j\right]$$
$$+ b_i(t) \tag{19}$$

with $\rho_i := \rho(x_i)$, $u_i(t) := u(x_i,t)$, $\beta_i := \beta(x_i)$, and $b_i(t) := b(x_i,t)$; furthermore, we replaced ε^2 by $N(N+1)(\Delta x)^2$ [35] with N representing the number of one-sided neighbor interactions. In addition, $u(x,t)$ is assumed twice differentiable for $x \notin \Omega_{PD}^0$ (cf. (12)). The quadrature implemented here, although it gives a rough approximation of the neighborhood boundary, produces a discrete model that is patch test consistent and is enough for the purpose of this paper.

We now observe that for $\beta \equiv 0$, (19) gives the CE model evaluated at x_i:

$$\rho_i\frac{\partial^2 u}{\partial t^2}(x_i,t) = K\frac{\partial^2 u}{\partial x^2}(x_i,t) + b_i(t),$$

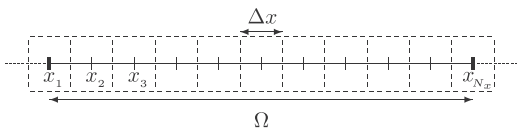whereas for $\beta \equiv 1$, (19) gives a nonlocal linear springs MD model for "particle" i:

Fig. 1. Discretization of a one-dimensional system.

$$m_i\frac{d^2 u_i}{dt^2}(t) = \sum_{\substack{j=-N\\j\neq 0}}^{N}\frac{2K}{N(N+1)}\frac{1}{|j\Delta x|}(u_{i+j}(t) - u_i(t)) + f_i^{\text{ext}}(t)$$

with $m_i := \rho_i\Delta x$, $f_i^{\text{ext}}(t) := b_i(t)\Delta x$, and $\sum_{j=1}^{N}j = \frac{N(N+1)}{2}$.

We now demonstrate that the discretized blended model (19) is patch test consistent. Assume a static problem with no external loads and let $u(x) = Fx + u_0$ with F and u_0 constant. Then, the right-hand side of (19) can be simplified as

$$\sum_{\substack{j=-N\\j\neq 0}}^{N}\left(\frac{\beta_i + \beta_{i+j}}{2}\right)\frac{1}{\Delta x}\frac{2K}{N(N+1)}\frac{1}{|j\Delta x|}Fj\Delta x - \frac{K}{\Delta x}F\left[\frac{2}{N(N+1)}\sum_{j=1}^{N}\left(\frac{\beta_{i+j} - \beta_{i-j}}{2}\right)\right]$$

which is identically zero.

In order to obtain a fully spatially discretized equation, we need to use an approximation for the spatial derivatives. We implement the centered finite differences

$$\frac{\partial u}{\partial x}(x_i,t) \approx \frac{u_{i+1}(t) - u_{i-1}(t)}{2\Delta x}, \tag{20}$$

$$\frac{\partial^2 u}{\partial x^2}(x_i,t) \approx \frac{u_{i+1}(t) - 2u_i(t) + u_{i-1}(t)}{\Delta x^2}, \tag{21}$$

and demonstrate that for the choice $N = 1$, (19) recovers a nearest-neighbor linear spring model. Indeed, we can write (19) in this case as

$$\rho_i\frac{d^2 u_i}{dt^2}(t) = \sum_{\substack{j=-1\\j\neq 0}}^{1}\left(\frac{\beta_i + \beta_{i+j}}{2}\right)\frac{K}{\Delta x}\frac{1}{|j\Delta x|}(u_{i+j}(t) - u_i(t))$$
$$- K\frac{1}{\Delta x}\frac{u_{i+1}(t) - u_{i-1}(t)}{2\Delta x}\left[\frac{\beta_{i+1} - \beta_{i-1}}{2}\right]$$
$$+ K\frac{u_{i+1}(t) - 2u_i(t) + u_{i-1}(t)}{\Delta x^2}\left[1 - \frac{\beta_i}{2} - \frac{1}{2}\frac{\beta_{i+1} + \beta_{i-1}}{2}\right]$$
$$+ b_i(t) = \frac{K}{\Delta x^2}(u_{i+1}(t) - 2u_i(t) + u_{i-1}(t)) + b_i(t).$$

The semi-discrete blended PD/CE model is then

$$\rho_i\frac{d^2 u_i}{dt^2} = \sum_{\substack{j=-N\\j\neq 0}}^{N}\left(\frac{\beta_i + \beta_{i+j}}{2}\right)\frac{1}{\Delta x}\frac{2K}{N(N+1)}\frac{1}{|j\Delta x|}(u_{i+j} - u_i)$$
$$- K\frac{1}{\Delta x}\frac{u_{i+1} - u_{i-1}}{2\Delta x}\left[\frac{2}{N(N+1)}\sum_{j=1}^{N}\left(\frac{\beta_{i+j} - \beta_{i-j}}{2}\right)\right]$$
$$+ K\frac{u_{i+1} - 2u_i + u_{i-1}}{\Delta x^2}\left[1 - \frac{\beta_i}{2} - \frac{1}{N(N+1)}\sum_{j=1}^{N}\frac{\beta_{i+j} + \beta_{i-j}}{2}j\right]$$
$$+ b_i, \tag{22}$$

where time dependence is omitted for brevity. The model (22) will be implemented below for numerical experiments.

4. Blending functions

In order to introduce the blending function $\beta(x)$, we first describe the decomposition of the domain Ω into subdomains for our one-dimensional system. Let us consider a domain $\Omega = (0,L)$. Given $0 < L_1 < L_2 < L_3 < L_4 < L$, we define

$$\Omega_{CE}^L := (0,L_1); \quad \Omega_b^L := (L_1,L_2); \quad \Omega_{PD} := (L_2,L_3);$$
$$\Omega_b^R := (L_3,L_4); \quad \Omega_{CE}^R := (L_4,L),$$

as shown in Fig. 2, and let $\Omega_{CE} = \Omega_{CE}^L \cup \Omega_{CE}^R$ and $\Omega_b = \Omega_b^L \cup \Omega_b^R$.

We define three types of blending functions: piecewise constant, piecewise linear, and piecewise cubic; these functions are shown in Fig. 3, using the parameters of Table 1.
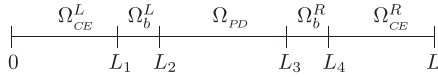
Fig. 2. Geometry of the one-dimensional system for the blended PD/CE model.

We now focus on the blended model (18), and observe that it can be written as follows:

$$\rho(x)\frac{\partial^2 u}{\partial t^2}(x,t) = \int_{-\varepsilon}^{\varepsilon} \left(\frac{\beta(x)+\beta(x+\xi)}{2}\right)\frac{2K}{\varepsilon^2}\frac{1}{|\xi|}(u(x+\xi,t)-u(x,t))d\xi$$
$$+ \bar{\beta}^{(1)}(x)K\frac{\partial u}{\partial x}(x,t) + \bar{\beta}^{(2)}(x)K\frac{\partial^2 u}{\partial x^2}(x,t) + b(x,t) \quad (23)$$

with

$$\bar{\beta}^{(1)}(x) := -\frac{2}{\varepsilon^2}\int_0^{\varepsilon}\left(\frac{\beta(x+\xi)-\beta(x-\xi)}{2}\right)d\xi, \quad (24)$$

$$\bar{\beta}^{(2)}(x) := 1 - \frac{\beta(x)}{2} - \frac{1}{\varepsilon^2}\int_0^{\varepsilon}\frac{\beta(x+\xi)+\beta(x-\xi)}{2}\xi d\xi. \quad (25)$$

We would like thus to investigate the support of $\bar{\beta}^{(1)}(x)$ and $\bar{\beta}^{(2)}(x)$ to understand the contribution of the spatial-derivative terms in (23). For that purpose, we define the discretized analogues of (24) and (25) as

$$\bar{\beta}_i^{(1)} := -\frac{1}{N(N+1)\Delta x}\sum_{j=1}^{N}(\beta_{i+j}-\beta_{i-j}), \quad (26)$$

$$\bar{\beta}_i^{(2)} := 1 - \frac{\beta_i}{2} - \frac{1}{2N(N+1)}\sum_{j=1}^{N}(\beta_{i+j}+\beta_{i-j})j, \quad (27)$$

and investigate their behavior for different choices of $\beta(x)$, specifically, piecewise constant, piecewise linear, and piecewise cubic, as in Fig. 3; for brevity, in the remaining of this paper, we will refer to "piecewise constant", "piecewise linear", and "piecewise cubic", as "constant", "linear", and "cubic", respectively. We choose a domain $\Omega = (0,1)$ and divide it into subdomains using the division presented in Fig. 2 with the parameters of Table 1; the horizon of the PD model is chosen as $\varepsilon = 0.05$. In Fig. 4, we illustrate the behavior of (a) $\bar{\beta}^{(1)}$ and (b) $\bar{\beta}^{(2)}$ using (26) and (27), respectively, computed in the entire domain, on a mesh with mesh size $\Delta x = 0.0001$ and with $N = \varepsilon/\Delta x = 500$. A close-up of these figures is presented in Figs. 4c and 4d, where transition regions between Ω_{PD} and Ω_b as well as between Ω_{CE} and Ω_b are emphasized.

We first observe that the support of $\bar{\beta}^{(1)}(x)$ extends beyond Ω_b to the subdomain $(L_1 - \varepsilon, L_2 + \varepsilon) \cup (L_3 - \varepsilon, L_4 + \varepsilon)$. This motivates the definition of the *transition domains*:

$$\Omega_t^L := (L_1 - \varepsilon, L_2 + \varepsilon),$$
$$\Omega_t^R := (L_3 - \varepsilon, L_4 + \varepsilon),$$
$$\Omega_t := \Omega_t^L \cup \Omega_t^R,$$

where Ω_t represents the supporting domain of $\bar{\beta}^{(1)}(x)$. In addition, we define the regions in which only the CE model is used as:

$$\Omega_{CE}^{0,L} := (0, L_1 - \varepsilon),$$
$$\Omega_{CE}^{0,R} := (L_4 + \varepsilon, L),$$
$$\Omega_{CE}^0 := \Omega_{CE}^{0,L} \cup \Omega_{CE}^{0,R},$$

Table 1
Geometric parameters for the blending functions in Fig. 3.

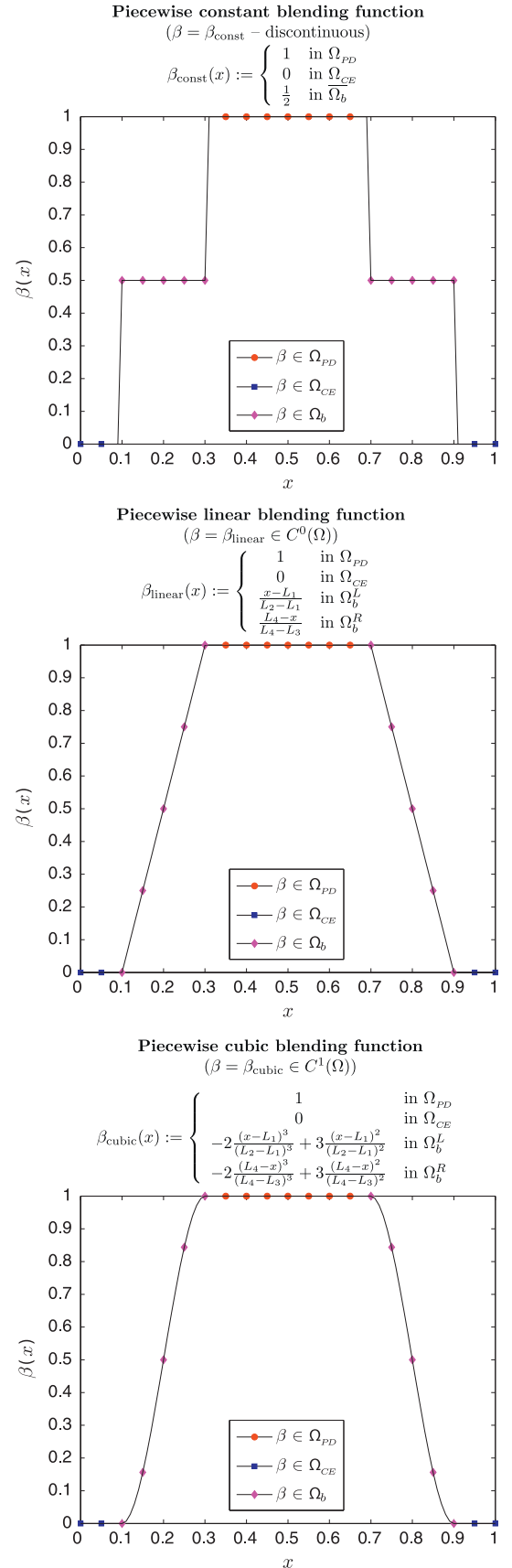| Ω	L_1	L_2	L_3	L_4
(0,1)	0.1	0.3	0.7	0.9

Fig. 3. Comparison between different blending functions: piecewise constant (top), piecewise linear (middle), and piecewise cubic (bottom). In each plot, an interpolation on a virtual fine mesh is used to approximate the continuous profile of the blending function; markers on a coarse mesh are included to indicate the different geometric regions.
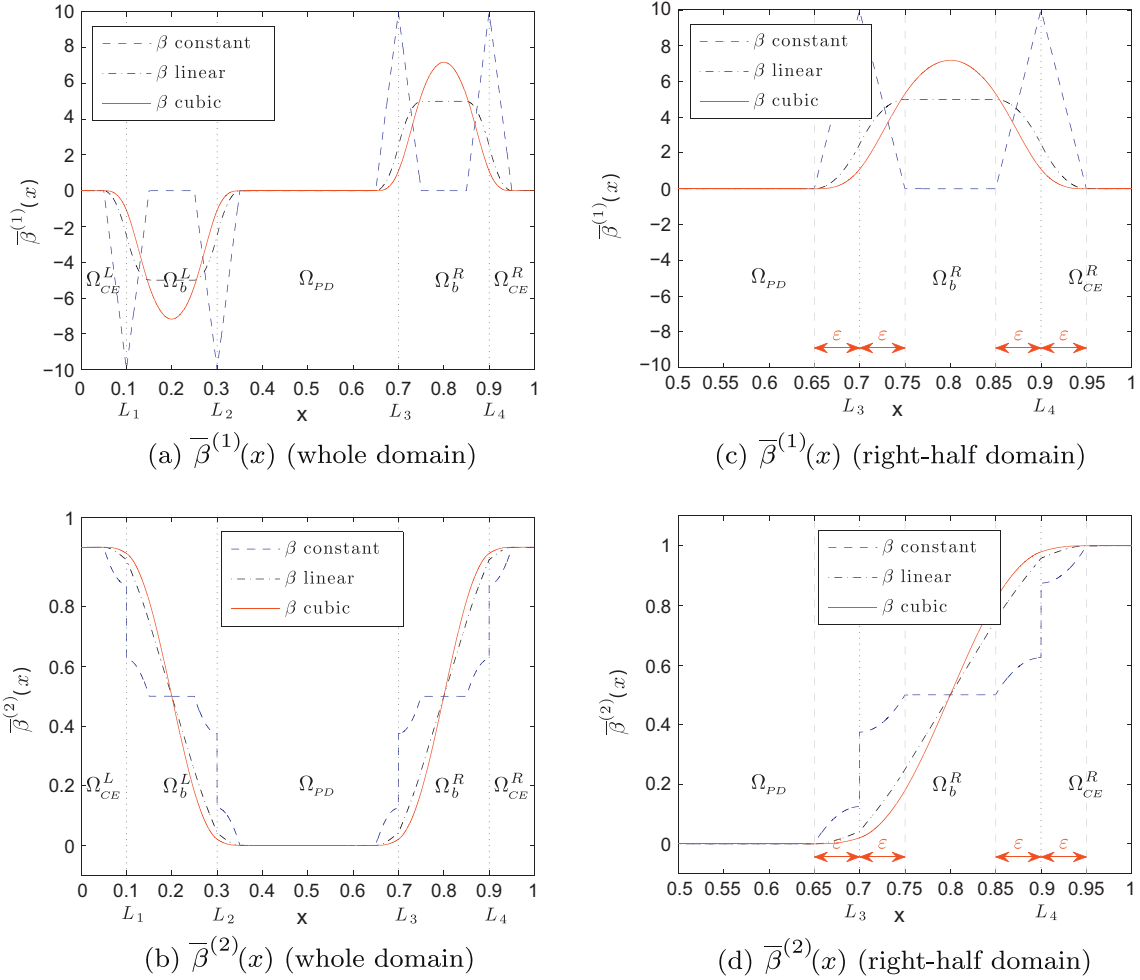
Fig. 4. Weights $\overline{\beta}^{(1)}(x)$ (a and c) and $\overline{\beta}^{(2)}(x)$ (b and d) in (23) approximated by (26) and (27), respectively. The computation of their profiles is performed with a resolution of $\Delta x = 0.0001$ for an horizon of $\varepsilon = 0.05$ with $N = \varepsilon/\Delta x = 500$. Figures (a and b) show the weights in the entire domain, whereas figures (c and d) zoom in on the right-half of the domain to emphasize the transition regions. The different subdomains are defined using the parameters of Table 1.

where Ω_{CE}^0 represents a "pure" CE domain; furthermore, we observe that $\Omega_{PD}^0 = (L_2 + \varepsilon, L_3 - \varepsilon)$ (cf. (11)), which represents a "pure" PD domain. In Fig. 5, we present the different subdomains.

5. Numerical experiments

In this section, we investigate numerically the behavior of the discretized blended PD/CE model (22) for static problems. In order to make an efficient implementation of the blended model, we first divide the nodes of the discrete system in three sets:

– Set I: nodes in Ω_{CE}^0;
– Set II: nodes in Ω_{PD}^0;
– Set III: nodes in Ω_t.

For that purpose, we define the following nodes:

$$i_{\text{ld}} = \max_i \{i : x_i < L_1 - N\Delta x\};$$
$$i_{\text{lu}} = \min_i \{i : x_i > L_2 + N\Delta x\};$$
$$i_{\text{rd}} = \max_i \{i : x_i < L_3 - N\Delta x\};$$
$$i_{\text{ru}} = \min_i \{i : x_i > L_4 + N\Delta x\}.$$

The nodes i_{ld}, i_{lu}, i_{rd}, and i_{ru} are illustrated in Fig. 6.

Following (22), the discretized equations of equilibrium for nodes in the three different sets above are:

Set I: ($i = 2, \ldots, i_{\text{ld}}, i_{\text{ru}}, \ldots, N_x - 1$)

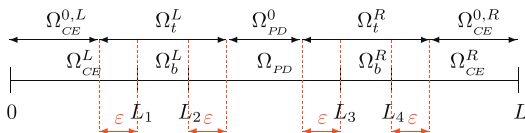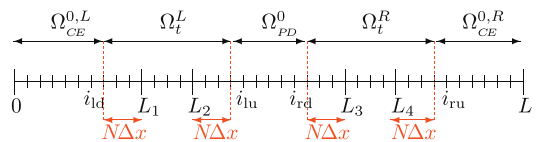$$K \frac{u_{i+1} - 2u_i + u_{i-1}}{\Delta x^2} = -b_i. \tag{28}$$

Fig. 5. Geometry of the one-dimensional system for the blended PD/CE model with transition regions Ω_t^L and Ω_t^R. The subdomains Ω_{PD}^0 and $\Omega_{CE}^0 := \Omega_{CE}^{0,L} \cup \Omega_{CE}^{0,R}$ represent "pure" PD and "pure" CE subdomains, respectively.

Fig. 6. Illustration of a one-dimensional system geometry for the blended PD/CE model with transition regions Ω_t^L and Ω_t^R. The nodes surrounding the left transition regions: i_{ld} and i_{lu}, and the ones surrounding the right transition region: i_{rd} and i_{ru}, are indicated; it is assumed that $N = 3$.

Set II: $(i = i_{lu}, \ldots, i_{rd})$

$$\sum_{\substack{j=-N \\ j \neq 0}}^{N} \frac{1}{\Delta x} \frac{2K}{N(N+1)} \frac{1}{|j\Delta x|} (u_{i+j} - u_i) = -b_i. \tag{29}$$

Set III: $(i = i_{ld} + 1, \ldots, i_{lu} - 1, i_{rd} + 1, \ldots, i_{ru} - 1)$

$$\sum_{\substack{j=-N \\ j \neq 0}}^{N} \left(\frac{\beta_i + \beta_{i+j}}{2} \right) \frac{1}{\Delta x} \frac{2K}{N(N+1)} \frac{1}{|j\Delta x|} (u_{i+j} - u_i)$$

$$- K \frac{1}{\Delta x} \frac{u_{i+1} - u_{i-1}}{2\Delta x} \left[\frac{2}{N(N+1)} \sum_{j=1}^{N} \left(\frac{\beta_{i+j} - \beta_{i-j}}{2} \right) \right]$$

$$+ K \frac{u_{i+1} - 2u_i + u_{i-1}}{\Delta x^2} \left[1 - \frac{\beta_i}{2} - \frac{1}{N(N+1)} \sum_{j=1}^{N} \frac{\beta_{i+j} + \beta_{i-j}}{2} j \right] = -b_i.$$

The construction of the stiffness matrix for the blended model (before imposing boundary conditions) is described in the pseudo-code in Algorithm A.

Algorithm A: Stiffness matrix assembly for blended PD/CE model

---

1: Initialize stiffness matrix A
2: Initialize blending function β {Note that $\beta = 0$ in Ω_{CE}}
3: {Assign blending function $\beta = 1$ in Ω_{PD}}
4: **for all** nodes i in Ω_{PD} **do**
5:     $\beta(i) = 1$
6: **end for**
7: {Evaluate blending function β in Ω_b}
8: **for all** nodes i in Ω_b **do**
9:     $\beta(i) = \beta\_function(x_i)$
10: **end for**
11: {Compute stiffness matrix in $\Omega_{CE}^0 := \Omega_{CE}^{0,L} \cup \Omega_{CE}^{0,R}$}
12: $f_{CE} = \frac{K}{\Delta x^2}$
13: **for all** nodes i in Ω_{CE}^0 **do**
14:     $A(i, i+1) = f_{CE}$
15:     $A(i, i) = -2 f_{CE}$
16:     $A(i, i-1) = f_{CE}$
17: **end for**
18: {Compute stiffness matrix in Ω_{PD}^0}
19: $f_{PD} = \frac{2K}{N(N+1)\Delta x^2}$
20: **for all** nodes i in Ω_{PD}^0 **do**
21:     **for** $j = 1$ to N **do**
22:         temp $= f_{PD}/j$
23:         $A(i, i+j) = $ temp
24:         $A(i, i) = A(i, i) - 2$ temp
25:         $A(i, i-j) = $ temp
26:     **end for**
27: **end for**
28: {Compute stiffness matrix in $\Omega_t := \Omega_t^L \cup \Omega_t^R$}
29: **for all** nodes i in Ω_t **do**
30:     SUM1 = 0
31:     SUM2 = 0
32:     {Compute nonlocal contributions}
33:     **for** $j = 1$ to N **do**
34:         temp $= f_{PD}/j$
35:         $A(i, i+j) = $ temp $\times \left(\frac{\beta(i)+\beta(i+j)}{2} \right)$
36:         $A(i, i) = A(i, i) - $ temp $\times \left(\frac{\beta(i+j)+2\beta(i)+\beta(i-j)}{2} \right)$
37:         $A(i, i-j) = $ temp $\times \left(\frac{\beta(i)+\beta(i-j)}{2} \right)$
38:         {Compute summations}
39:         SUM1 = SUM1 + $(\beta(i+j) - \beta(i-j))$
40:         SUM2 = SUM2 + $(\beta(i+j) + \beta(i-j)) \times j$
41:     **end for**
42:     SUM1 $= \frac{f_{PD}}{4} \times$ SUM1
43:     SUM2 $= f_{CE} \times \left(1 - \frac{\beta(i)}{2} - \frac{1}{2N(N+1)} \text{SUM2} \right)$
44:     {Compute local contributions}
45:     {Contributions of first derivative term}
46:     $A(i, i+1) = A(i, i+1) - $ SUM1
47:     $A(i, i-1) = A(i, i-1) + $ SUM1
48:     {Contributions of second derivative term}
49:     $A(i, i+1) = A(i, i+1) + $ SUM2
50:     $A(i, i) = A(i, i) - 2$ SUM2
51:     $A(i, i-1) = A(i, i-1) + $ SUM2
52: **end for**

The blended PD/CE model will be compared with classical CE and PD models in their discretized forms (28) and (29), respectively, applied to the entire domain. Dirichlet boundary conditions are imposed on $u(0)$ and $u(L)$ for the CE and blended PD/CE models. For the PD model, the boundary of the domain is extended to a nonlocal boundary layer, so that additional $N - 1$ nodes are added to the left and to the right sides of the domain; boundary conditions are then imposed on u_i, $i = -(N-2), \ldots, 1, N_x, \ldots, N_x + (N-1)$, using the solution of the CE model as boundary condition.

5.1. Static problems with no external load

In the following, we present results for the case of no external load for Dirichlet boundary conditions. Since it is simple to verify that $u(x, t) = 0$ is a solution of (15) by inspection, and the midpoint quadrature rule used for discretization exactly integrates constants avoiding quadrature errors, we focus on *non-homogeneous* Dirichlet boundary conditions. The geometrical and material parameters are presented in Table 2.

The main purpose of these experiments is to demonstrate numerically the efficacy of the blended model in terms of patch test consistency. We compare the CE, PD, and blended PD/CE models for different choices of blending functions (constant, linear, and cubic). In each case, we compare the displacement profiles between the different models; the average strain corresponding to the interval $[x_i, x_{i+1}]$, $i = 1, \ldots, N_x - 1$, is computed as

$$\frac{du}{dx}(x_i) = \frac{u_{i+1} - u_i}{x_{i+1} - x_i}.$$

In addition, we compute the following measure to estimate the accuracy in the strain:

$$\Delta \epsilon = \max_i \left| \frac{du}{dx}(x_i) \right| - \min_i \left| \frac{du}{dx}(x_i) \right|. \tag{30}$$

In Fig. 7 we present numerical results showing the displacement profiles for non-homogeneous Dirichlet boundary conditions with $u(0) = 0$ and $u(L) = 1$, respectively. On each subfigure caption, we indicate the value of $\Delta \epsilon$ described in (30).

We observe that a linear profile is produced by the blended PD/CE model, as expected, as in the PD and CE models. In other words,

Table 2
Geometrical and material parameters for the numerical experiments with no external load.

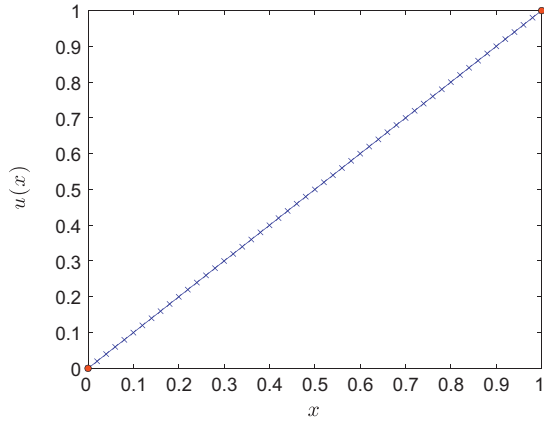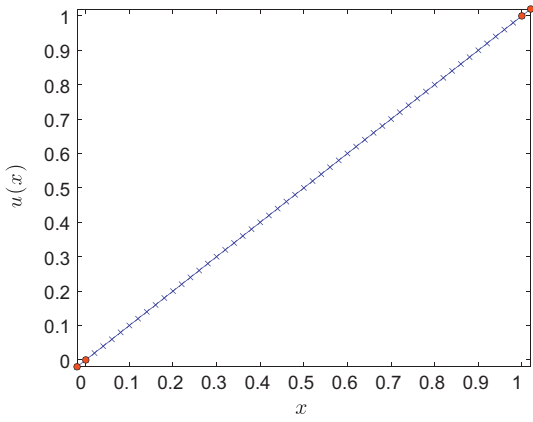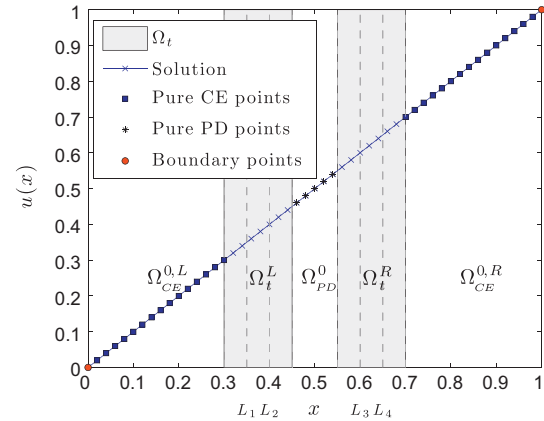| Ω	L_1	L_2	L_3	L_4	K	ε	Δx
$(0, 1)$	0.35	0.4	0.6	0.65	1	0.05	0.02

(a) Classical Elasticity: $\Delta\varepsilon = 2.76e-14$

(b) Peridynamics: $\Delta\varepsilon = 1.22e-12$

(c) Blended PD/CE: $\Delta\varepsilon = 3.33e-14$ (constant)
$\Delta\varepsilon = 3.69e-14$ (linear)
$\Delta\varepsilon = 4.31e-14$ (cubic)

Fig. 7. Displacement profile comparison for the case of no external load with Dirichlet boundary conditions $u(0) = 0$ and $u(1) = 1$: (a) classical elasticity, (b) peridynamics, and (c) blended PD/CE model with cubic blending function $\beta(x)$; the displacement profile for constant and linear blending functions looks qualitatively identical to (c). In all figures, the red circles represent nodes where boundary conditions are imposed. In (c), transition regions are shaded by gray, nodes in the "pure" PD region Ω_{PD}^0 are represented by black stars, and nodes in the "pure" CE region Ω_{CE}^0 are represented by blue squares. The accuracy in the strain, measured by $\Delta\epsilon$ in (30), is shown in the caption of each figure; in (c) we present the accuracy in the strain for the three blending functions. The simulations use the parameters presented in Table 2.

we demonstrated numerically that the blended PD/CE model is patch test consistent. In Fig. 8, we present the oscillations in the strain around the theoretical value of $\frac{du}{dx} = 1$; we observe that the errors in the strain for the CE and blended PD/CE models are *round-off errors*. In the case of the PD model, we have an additional source of error in the strain related to the *nonlocal* boundary conditions.

5.2. Static problems with a point load

In Section 5.1, we demonstrated that the blended model is patch test consistent and, in particular, gives the same numerical result as the PD and CE models, which produce identical solutions under consistent boundary conditions. Problems of interest for the implementation of the blended PD/CE model involve situations in which the PD model would be computationally too expensive to solve everywhere and could be replaced by the CE model in some regions without deteriorating the accuracy in the prediction of quantities of interest. Such situations occur whenever the CE model provides reasonable large-scale approximations of the PD model.

To test the performance of the blended model in a non-trivial situation, we apply a point load to the system, i.e., $b(x) = \delta(x - x_p)$, with $\delta(x)$ the Dirac delta function and x_p the location where the point load is applied. Numerically, we implement this load as $b_i = \delta_{ip}/\Delta x$ with δ_{ip} the Kronecker's delta, p the node number where the load is applied, and Δx the mesh resolution. We run numerical simulations using the parameters of Table 3, with p the node at the center of the domain.

In order to estimate the accuracy of the blended PD/CE numerical solution with respect to the PD solution, we introduce two standard discrete error measures as follows. Given a vector $\mathbf{v}$ with components $v_i, i = 1, \ldots, N_x$, we define:

– the ℓ^∞ norm

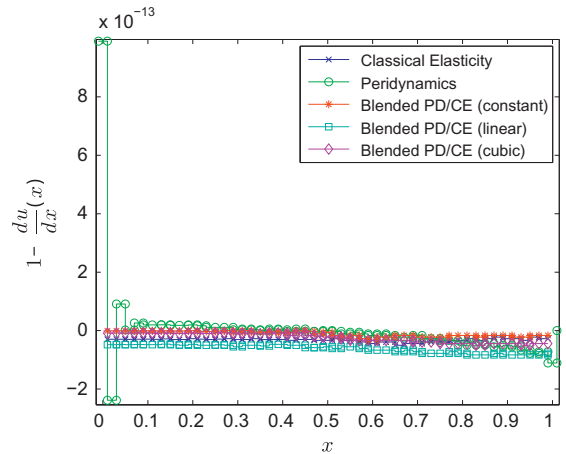$$\|\mathbf{v}\|_{\ell^\infty} := \max_{i=1,\ldots,N_x} |v_i|, \tag{31}$$

Fig. 8. Strain fluctuation around $du/dx = 1$ for the different models, for the case of no external load with Dirichlet boundary conditions $u(0) = 0$ and $u(1) = 1$. The simulations use the parameters presented in Table 2.

Table 3
Geometrical and material parameters for the numerical experiments with point loads.

Ω	L_1	L_2	L_3	L_4	K	ε	Δx
$(0,1)$	0.12	0.25	0.75	0.88	1	0.05	1/300

– the ℓ^2 norm

$$\|\mathbf{v}\|_{\ell^2} := \sqrt{\sum_{i=1}^{N_x} |v_i|^2}. \tag{32}$$

Let $\mathbf{u}$ and $\mathbf{u}^{PD}$ be the vectors of the numerical solution at the nodes for the blended PD/CE model and the PD model, respectively. Then, we define the error in the numerical solution as $\mathbf{e} = \mathbf{u}^{PD} - \mathbf{u}$ and the measures of the *relative error* in the ℓ^∞ and ℓ^2 norms, respectively, as

$$e_{r,\infty} := \frac{\|\mathbf{e}\|_{\ell^\infty}}{\|\mathbf{u}^{PD}\|_{\ell^\infty}}, \tag{33}$$

$$e_{r,2} := \frac{\|\mathbf{e}\|_{\ell^2}}{\|\mathbf{u}^{PD}\|_{\ell^2}}. \tag{34}$$

We compare as well the numerical solution of the PD model with both the numerical solution and the exact solution of the CE model, which can be calculated as

$$u_{CE}(x) = \begin{cases} u(x_0) + \frac{du}{dx}(x_0)(x - x_0) & x_0 < x \leqslant x_p, \\ u(x_L) - \frac{du}{dx}(x_L)(x_L - x) & x_p < x < x_L, \end{cases}$$

where the values of $u(x_0)$ and $u(x_L)$ are provided as boundary conditions and the derivatives are given by

$$\frac{du}{dx}(x_0) = \frac{u(x_L) - u(x_0)}{x_L - x_0} + \frac{1}{K} \frac{x_L - x_p}{x_L - x_0},$$

$$\frac{du}{dx}(x_L) = \frac{du}{dx}(x_0) - \frac{1}{K}.$$

In Fig. 9, we compare the PD solution with the blended PD/CE solutions (a and b) and the CE solution (c and d). In (a and c) the comparison is presented in the entire domain, whereas in (b and d) we zoom in around the point load to better illustrate the displacement behavior. The comparison between PD and blended PD/CE models (a and b) are performed for three different blending functions: constant, linear, and cubic (cf. Fig. 3). We observe that, in this case, the CE numerical solution recovers the CE exact solution, but differs from the PD solution; the blended models, on the other hand, reproduce the PD solution profile.

In Fig. 10, we plot the absolute value of the difference between the blended PD/CE solution and the PD solution at each node. In (a) we use a normal-log scale to be able to compare the error produced by the three blending functions. In (b–d) we present the errors produced by each of the blending functions separately, using different scales for the y-axis on each plot. We observe that, in this case, the cubic blending function performs better than the linear one, which gives itself lower errors than the constant one. In the captions of (b–d) we also present the relative error in the ℓ^∞ and ℓ^2 norms, as described in (33) and (34), respectively.
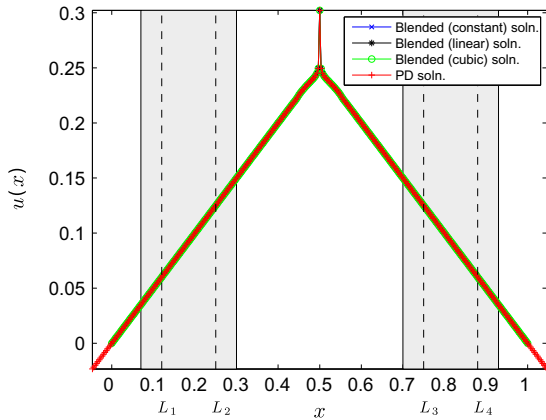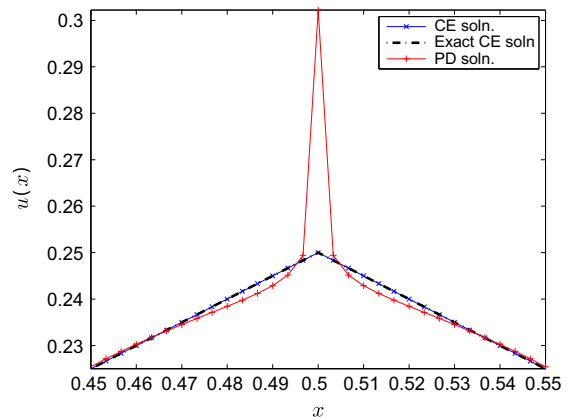

(a) PD vs. Blended PD/CE (whole domain)
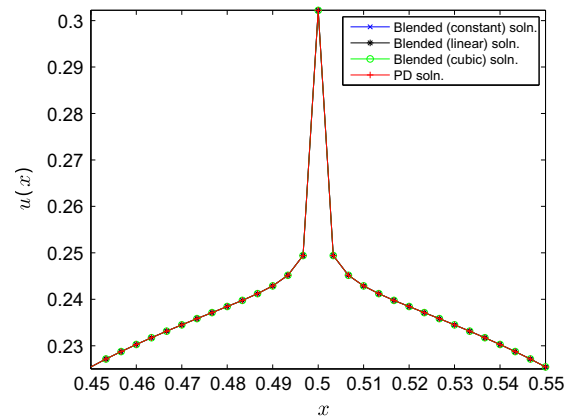
(b) PD vs. Blended PD/CE (close-up)
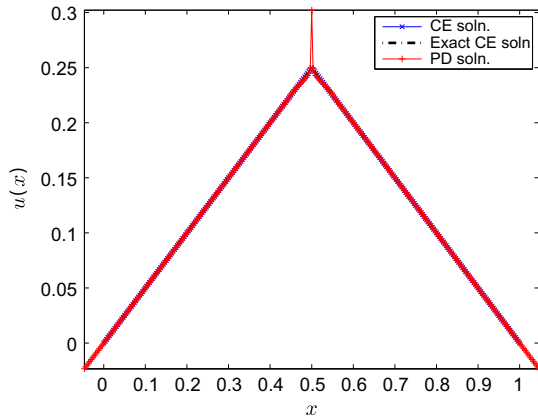
(c) PD vs. CE (whole domain)

(d) PD vs. CE (close-up)

Fig. 9. Displacement comparison for the case of a point load with Dirichlet boundary conditions $u(0) = u(1) = 0$. We compare the PD and blended PD/CE models in the whole domain (a) as well as around the point load (b). A comparison of the PD and CE models in the whole domain (c) and around the point load (d) is also shown. The blended PD/CE model reproduces the solution of the PD model, whereas the CE model gives a different result, consistent with the exact CE solution. The simulations use the parameters presented in Table 3.
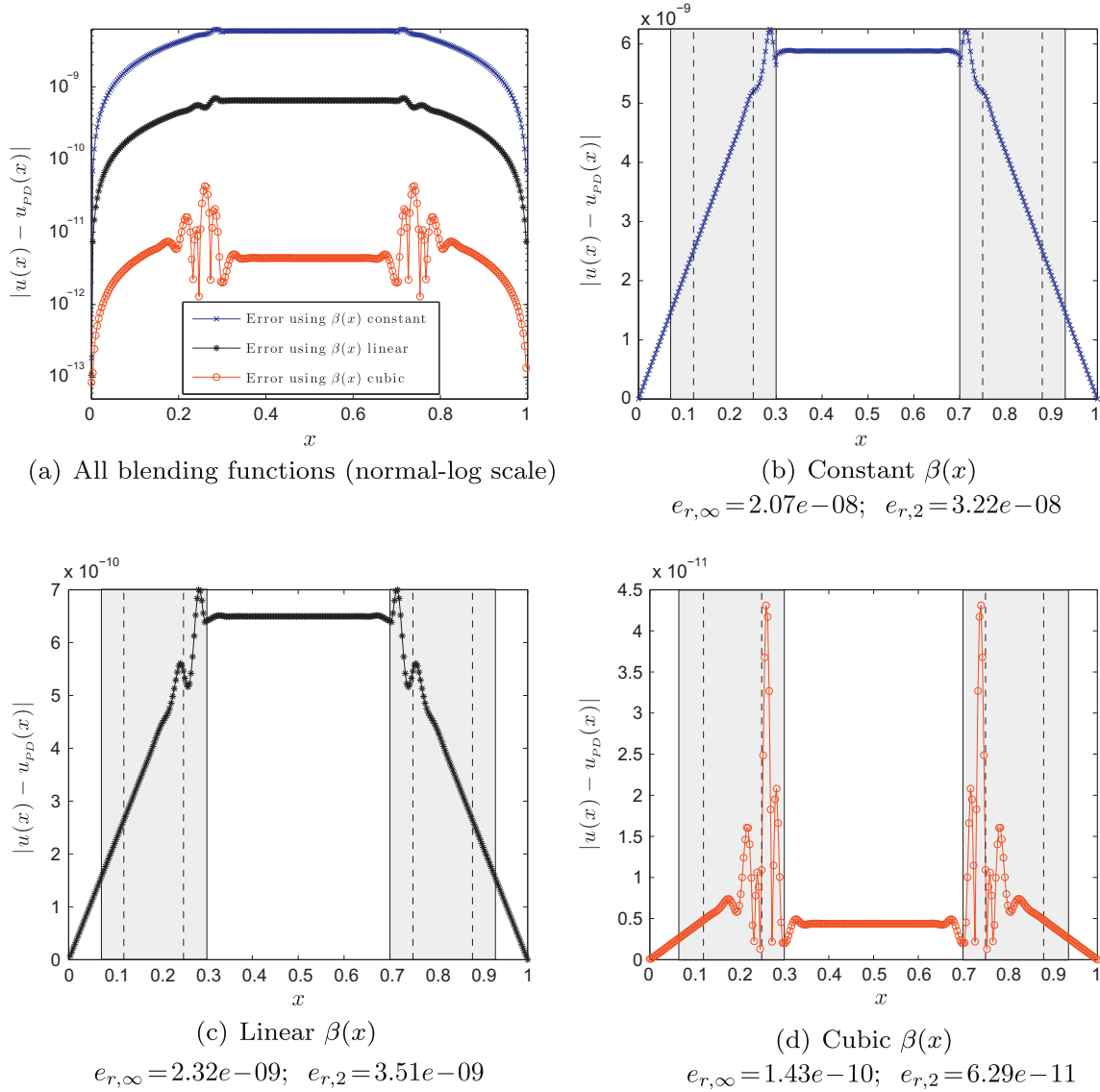
(a) All blending functions (normal-log scale)

(b) Constant $\beta(x)$
$$e_{r,\infty} = 2.07e-08; \quad e_{r,2} = 3.22e-08$$

(c) Linear $\beta(x)$
$$e_{r,\infty} = 2.32e-09; \quad e_{r,2} = 3.51e-09$$

(d) Cubic $\beta(x)$
$$e_{r,\infty} = 1.43e-10; \quad e_{r,2} = 6.29e-11$$

Fig. 10. Error profiles for the blended PD/CE models with respect to the numerical solution to the PD model: (a) Comparison of the solutions for the three different blending functions in a normal-log scale; (b–d) profiles for a particular blending function. The solution to the PD model is represented by $u_{PD}(x)$, whereas the solution to the blended PD/CE model is represented by $u(x)$. Note that the y-axis scales in (b–d) differ.

5.2.1. Error sensitivity on PD region size

We have demonstrated the efficacy of the blended model for problems involving point loads. In this section, we investigate the behavior of the error in the presence of a point load as a function of the size of the PD region, i.e., $|\Omega_{PD}| = L_3 - L_2$. In the following simulations, we choose, as in Table 3, $\Omega = (0,1)$ and $K = 1$. We run experiments for two values of the horizon: $\varepsilon = \varepsilon_1 = 0.05$ (as in Table 3) and $\varepsilon = \varepsilon_2 = 0.025$, and choose fixed spatial resolutions of $\Delta x = 0.0005$ and $\Delta x = 0.00025$, respectively, to retain accuracy in the spatial integration (see, e.g., the δ-convergence analysis in [10,12]). In this case, we vary the size of Ω_{PD}, while fixing the length of the bridging regions: $|\Omega_b^L| = L_2 - L_1 = |\Omega_b^R| = L_4 - L_3 = 0.1$.

Results for each of the horizons are presented in Fig. 11. In each case, we vary $|\Omega_{PD}|$ by $2\Delta x$. The left plots (a and c) show the relative error in the ℓ^2 norm for each horizon as a function of the PD region size, for the three blending functions. We observe that the error has a decreasing tendency with the size of the PD region, although oscillations in the error are present. These oscillations are related to the nature of the PD solution, as we can observe in (b and d), where the difference between the solution to the PD

model and the solution to the CE model is presented, for each horizon.

Remark 6. Fig. 11 demonstrates that a significant decrease in the error magnitude can be achieved by changing the PD region size. Changing the PD domain implies a change in the multiscale model used. In other words, the question about the size of the PD region is a modeling question and should be treated as a modeling error problem.

5.2.2. Error sensitivity on bridge size

In this section, we would like to investigate the behavior of the error with respect to the size of the bridge regions, i.e., $|\Omega_b^L| = L_2 - L_1 = |\Omega_b|/2$ and $|\Omega_b^R| = L_4 - L_3 = |\Omega_b|/2$, while keeping the PD region fixed, i.e., $|\Omega_{PD}| = L_3 - L_2$ constant. As in Section 5.2.1, we run experiments for the cases of $\varepsilon = \varepsilon_1 = 0.05$ and $\varepsilon = \varepsilon_2 = 0.025$, with grid resolutions of $\Delta x = 0.0005$ and $\Delta x = 0.00025$, respectively. We choose to fix the size of the PD region to be $|\Omega_{PD}| = 2\varepsilon - 6\Delta x$ on each case. Furthermore, $\Omega = (0,1)$ and $K = 1$.
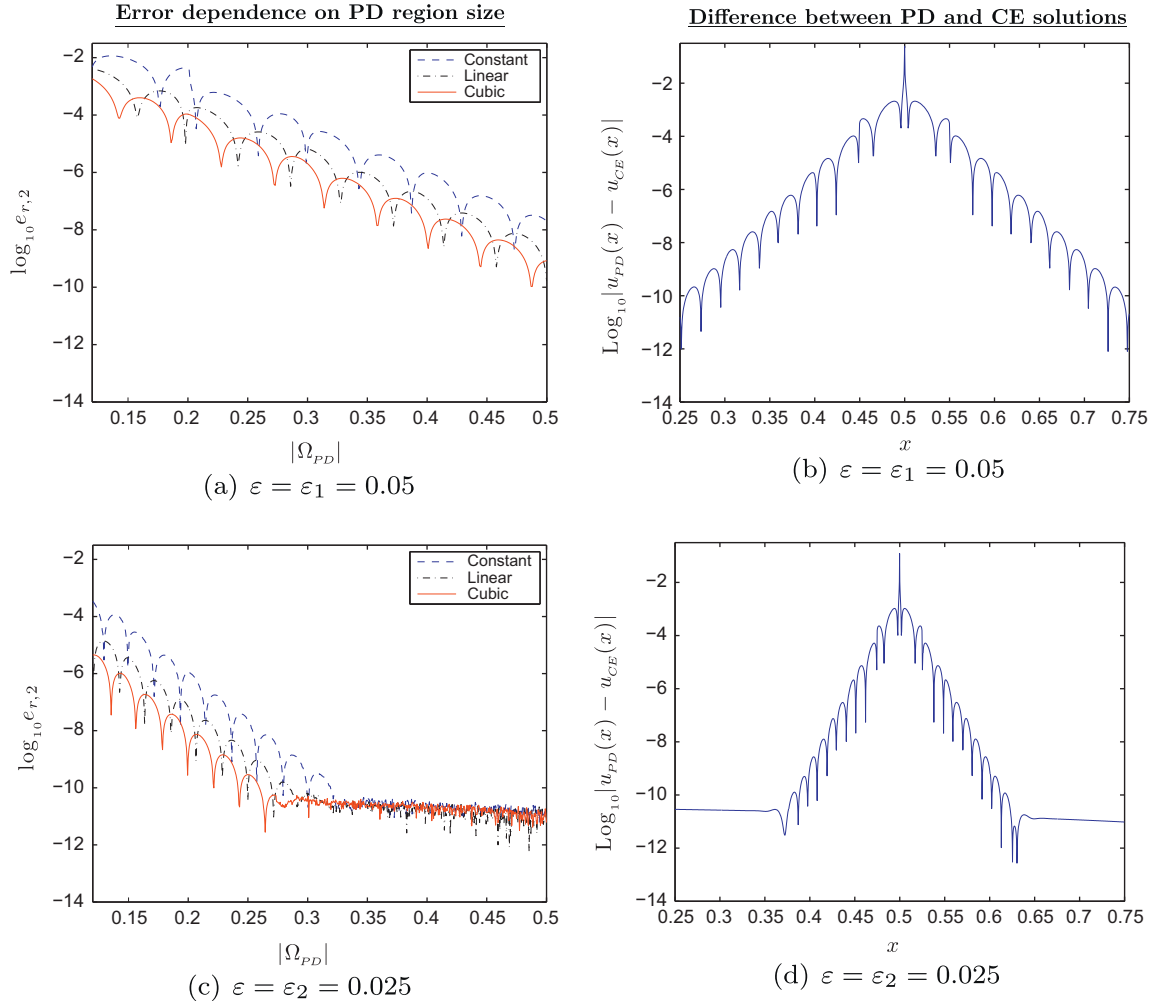
Error dependence on PD region size

(a) $\varepsilon = \varepsilon_1 = 0.05$

Difference between PD and CE solutions

(b) $\varepsilon = \varepsilon_1 = 0.05$

(c) $\varepsilon = \varepsilon_2 = 0.025$

(d) $\varepsilon = \varepsilon_2 = 0.025$

Fig. 11. Left: Error dependence on the PD region size. Right: Difference between PD and CE solutions. The top plots correspond to simulations using a horizon of $\varepsilon = \varepsilon_1 = 0.05$, whereas the bottom plots correspond to simulations using a horizon of $\varepsilon = \varepsilon_2 = 0.025$. In (a and c), we show the relative error in the ℓ^2 norm, for each horizon, as a function of the PD region size. In (b and d), we plot the difference between the solution to the PD model and the solution to the CE model, for each horizon.

The results showing the relative error in the ℓ^2 norm for each horizon as a function of the bridge region size, for the three blending functions, are presented in Fig. 12. We observe that in the case of linear and cubic blending functions, the error eventually decreases monotonically, for $|\Omega_b| > 2\varepsilon$ (i.e., $|\Omega_b^L| = |\Omega_b^R| > \varepsilon$). On the contrary, for a constant blending function the error does not appear to be sensitive to the bridge size.

5.2.3. Error sensitivity on point load location

An important consideration on bridging methods is not only the size of the bridge but also its position. Here we investigate how the location of the point load with respect to the center of the PD region affects the error. For that purpose, we choose $\Omega = (0,1)$, $K = 1$, $\varepsilon = 0.05$, $\Delta x = 0.005$, $|\Omega_b^L| = |\Omega_b^R| = \varepsilon$ and $|\Omega_{PD}| = 6\varepsilon$.

Fig. 13, shows the sensitivity of the accuracy of the blended PD/CE model solution on the point load location. In (a), we present results for the relative error in the ℓ^2 norm as a function of the point load location, for the three blending functions. In (b–f) we present simultaneously the numerical solutions for the displacement profile for different point loads for the different models as follows: (b) CE model, (c) PD model, (d–f) blended PD/CE model with constant, linear, and cubic blending function, respectively. In (a), we observe that a significant error is obtained if the point load is in the transition region; once the point load is located inside the

"pure" PD region, the error decreases significantly (up to 4 orders of magnitude) whenever the point load location gets closer to the center of the "pure" PD region. We also observe that the blended PD/CE model solution resembles either the CE or the PD solutions when the point load is in the "pure" CE or "pure" PD regions, respectively. Furthermore, we note that in the case of the constant blending function, large errors are obtained when the point load is in the transition region, in comparison to the linear and cubic cases.

5.2.4. Efficiency of the blended PD/CE model

We study the computational cost of the blended PD/CE model with respect to the PD model. For that purpose, we choose, as in Section 5.2.3, $\Omega = (0,1)$, $K = 1$, $\varepsilon = 0.05$, and $|\Omega_{PD}| = 6\varepsilon$. To have further impact in the time reduction, we use a very fine mesh with $\Delta x = 0.0001$; however, we choose $|\Omega_b^L| = |\Omega_b^R| = 3\Delta x$, in order to reduce the computational cost in the transition regions.

In order to demonstrate the efficiency of our method, we coarsen the grid in the "pure" CE region with a resolution of $\Delta x_{CE} \geqslant \Delta x$. As a consequence, we replace the centered finite differences scheme in (21) by one for non-uniform meshes:

$$\frac{\partial^2 u}{\partial x^2}(x_i, t) \approx 2 \frac{\Delta x_i u_{i+1} - (\Delta x_{i+1} + \Delta x_i) u_i + (\Delta x_{i+1}) u_{i-1}}{\Delta x_i (\Delta x_{i+1} + \Delta x_i) \Delta x_{i+1}},$$
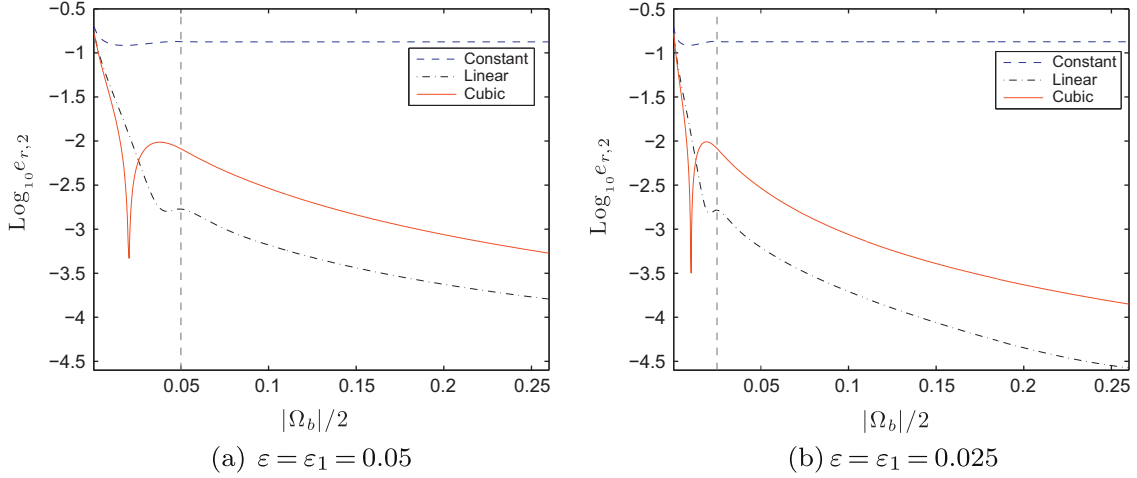
Fig. 12. Relative error in the ℓ^2 norm as a function of the bridge region size, i.e., $|\Omega_b|/2 = L_2 - L_1 = L_4 - L_3$. Figure (a) is computed with $\varepsilon = \varepsilon_1 = 0.05$ and figure (b) is computed with $\varepsilon = \varepsilon_2 = 0.025$, with grid resolutions of $\Delta x = 0.0005$ and $\Delta x = 0.00025$, respectively. The length of the bridge region varies by Δx in each case. Results show the evolution of the error for the different blending functions: constant, linear, and cubic.

where $\Delta x_i := x_i - x_{i-1}$ and the time dependence on the right-hand side is omitted for brevity. The relative error in the ℓ^2 norm is replaced by a *weighted* relative error:

$$e^w_{r,2} := \frac{\sqrt{\sum_{i=2}^{N_x-1}(e_i)^2 \Delta x_i}}{\sqrt{\sum_{i=2}^{N_x-1}(u_i^{PD})^2 \Delta x_i}} \qquad (35)$$

with weights $\Delta x_i := \frac{x_{i+1}-x_{i-1}}{2}$, and where $e_i = u_i^{PD} - u_i$; u_i^{PD} and u_i are the solutions at node i of the PD and blended PD/CE models, respectively. Furthermore, given the computational times t_{PD} and $t_{Blended}$ that are necessary to solve for the PD solution and blended PD/CE solution (with cubic blending functions), respectively, we define the speedup as $t_{PD}/t_{Blended}$ and compute it in MatLab.

Fig. 14 shows the results for the errors and speedup as a function of the "pure" CE relative mesh size. We first show in (a) that the PD model gives a solution that differs from the CE exact solution, whereas in (b) we see that the PD solution can be recovered by the blended PD/CE model. We present in (c) the error behavior as a function of the "pure" CE relative mesh size, i.e., $\Delta x_{CE}/\Delta x$; in (d) the speedup profile is shown. The results here are twofold:

1. Coarsening the pure CE domain mesh does not affect significantly the error.
2. A speedup of up to ~18 is obtained by coarsening the mesh in the "pure" CE domain.

Remark 7. The errors and speedup not only depend on the pure CE mesh size, but also on other components of the blended PD/CE model such as the bridge region and PD region sizes.

6. Blending peridynamics with higher-order gradient models

The implemented methodology in Section 3.2 to couple PD and CE can be generalized to derive blending schemes to couple PD and higher-order gradient models (HOGMs). Assume that for any $x \notin \Omega_{PD}^0$ the displacement field is smooth up to order M so that the following approximation is valid:

$$u(x',t) - u(x,t) \approx \sum_{n=1}^{M} \frac{1}{n!} \frac{\partial^n u}{\partial x^n}(x,t)(x'-x)^n, \quad |x'-x| \leqslant \varepsilon. \qquad (36)$$

Then, we can write (6) as

$$\rho(x)\frac{\partial^2 u}{\partial t^2}(x,t) = \int_{-\varepsilon}^{\varepsilon}\left(\frac{\beta(x)+\beta(x+\xi)}{2}\right)C(|\xi|)(u(x+\xi,t)-u(x,t))d\xi$$
$$+ \sum_{n=1}^{M}\frac{\partial^n u}{\partial x^n}(x,t)\frac{1}{n!}\int_{-\varepsilon}^{\varepsilon}\left(1-\frac{\beta(x)+\beta(x+\xi)}{2}\right)C(|\xi|)\xi^n d\xi$$
$$+ b(x,t).$$

We now observe that

$$\int_{-\varepsilon}^{\varepsilon}\left(1-\frac{\beta(x)+\beta(x+\xi)}{2}\right)C(|\xi|)\xi^n d\xi$$
$$= (1+(-1)^n)\left(1-\frac{\beta(x)}{2}\right)\int_{0}^{\varepsilon}C(|\xi|)\xi^n d\xi$$
$$- \int_{0}^{\varepsilon}\left(\frac{\beta(x+\xi)+(-1)^n\beta(x-\xi)}{2}\right)C(|\xi|)\xi^n d\xi.$$

Thus, assuming M even,

$$\rho(x)\frac{\partial^2 u}{\partial t^2}(x,t) = \int_{-\varepsilon}^{\varepsilon}\left(\frac{\beta(x)+\beta(x+\xi)}{2}\right)C(|\xi|)(u(x+\xi,t)$$
$$- u(x,t))d\xi - \sum_{k=1}^{M/2}\frac{\partial^{2k-1}u}{\partial x^{2k-1}}(x,t)\frac{1}{(2k-1)!}$$
$$\left[\int_{0}^{\varepsilon}\left(\frac{\beta(x+\xi)-\beta(x-\xi)}{2}\right)C(|\xi|)\xi^{2k-1}d\xi\right]$$
$$+ \sum_{k=1}^{M/2}\frac{\partial^{2k}u}{\partial x^{2k}}(x,t)\frac{1}{(2k)!}\left[2\left(1-\frac{\beta(x)}{2}\right)\int_{0}^{\varepsilon}C(|\xi|)\xi^{2k}d\xi\right.$$
$$\left. - \int_{0}^{\varepsilon}\left(\frac{\beta(x+\xi)+\beta(x-\xi)}{2}\right)C(|\xi|)\xi^{2k}d\xi\right] + b(x,t). \qquad (37)$$

As an example, let $M = 4$. Then, (37) gives

$$\rho(x)\frac{\partial^2 u}{\partial t^2}(x,t) = \int_{-\varepsilon}^{\varepsilon}\left(\frac{\beta(x)+\beta(x+\xi)}{2}\right)C(|\xi|)(u(x+\xi,t)-u(x,t))d\xi$$
$$- \frac{\partial u}{\partial x}(x,t)\left[\int_{0}^{\varepsilon}\left(\frac{\beta(x+\xi)-\beta(x-\xi)}{2}\right)C(|\xi|)\xi d\xi\right]$$
$$+ \frac{\partial^2 u}{\partial x^2}(x,t)\left[K\left(1-\frac{\beta(x)}{2}\right)-\frac{1}{2}\int_{0}^{\varepsilon}\left(\frac{\beta(x+\xi)+\beta(x-\xi)}{2}\right)\right.$$
$$\left. \times C(|\xi|)\xi^2 d\xi\right] - \frac{\partial^3 u}{\partial x^3}(x,t)\left[\frac{1}{3!}\int_{0}^{\varepsilon}\left(\frac{\beta(x+\xi)-\beta(x-\xi)}{2}\right)\right.$$
$$\left. \times C(|\xi|)\xi^3 d\xi\right] + \frac{\partial^4 u}{\partial x^4}(x,t)\left[\kappa\left(1-\frac{\beta(x)}{2}\right)-\frac{1}{4!}\right.$$
$$\left. \times \int_{0}^{\varepsilon}\left(\frac{\beta(x+\xi)+\beta(x-\xi)}{2}\right)C(|\xi|)\xi^4 d\xi\right] + b(x,t) \qquad (38)$$
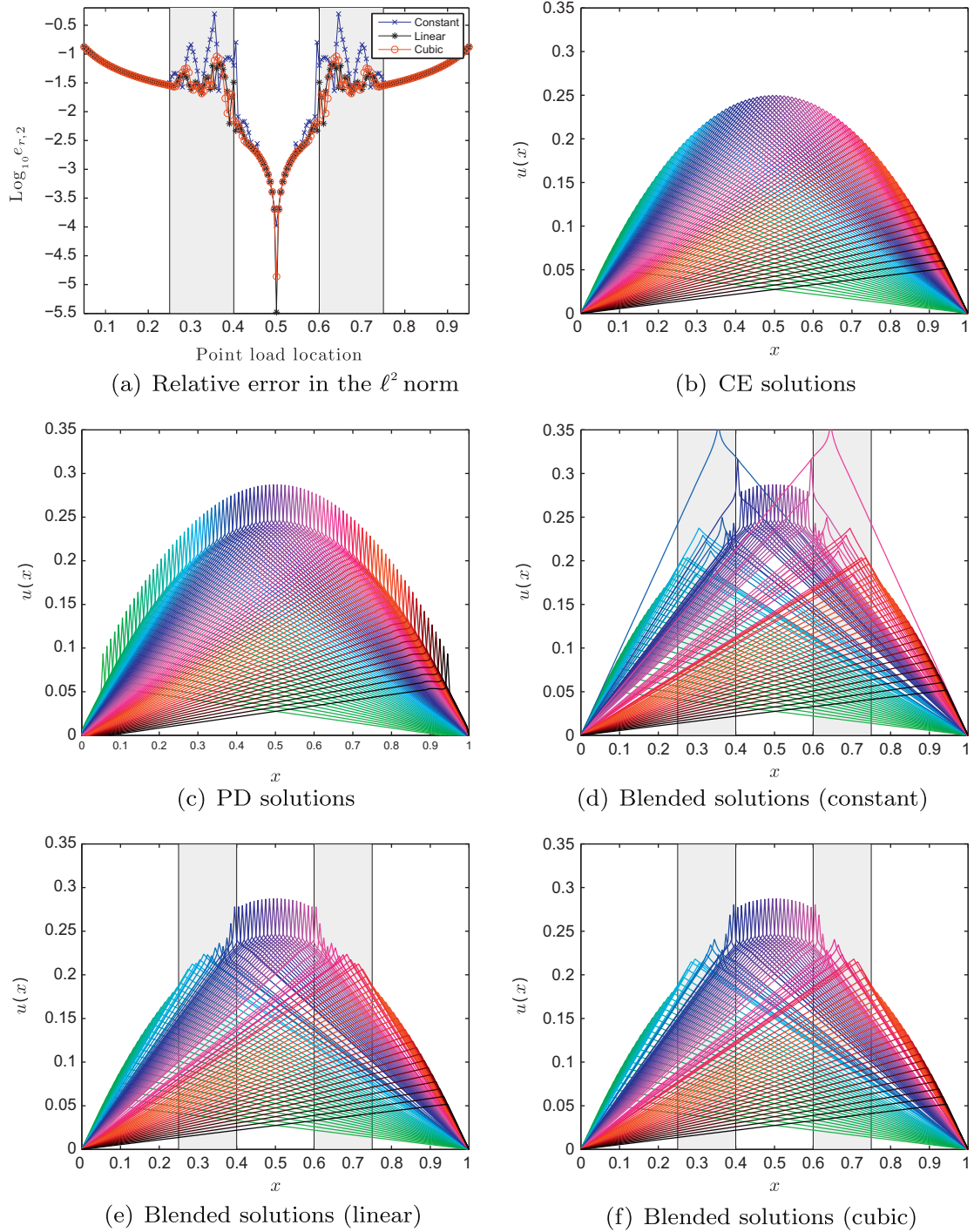
Fig. 13. System sensitivity with respect to the location of the point load. (a) Relative error in the ℓ^2 norm as a function of the position of the point load for the different blending functions: constant, linear, and cubic. (b) Solutions of the CE model, (c) solutions of the PD model, (d–f) solutions of the blended PD/CE model for constant, linear, and cubic blending functions, respectively. In (b–e) we plot half of the solutions presented in (a).

with K given in (7) and

$$\kappa := \frac{1}{12} \int_0^\varepsilon C(|\xi|)\xi^4 d\xi. \tag{39}$$

For $\beta \equiv 1$, (38) recovers the PD model (6). For $\beta \equiv 0$, (38) gives the higher-order gradient model

$$\rho(x)\frac{\partial^2 u}{\partial t^2}(x,t) = K\frac{\partial^2 u}{\partial x^2}(x,t) + \kappa\frac{\partial^4 u}{\partial x^4}(x,t) + b(x,t). \tag{40}$$

Remark 8. We observe that the blended model (37) gives for $\beta \equiv 0$ a higher-order gradient model composed of only even derivatives of the displacement field; in addition, the micromodulus choice (17) gives $\kappa = K\varepsilon^2/24$ in (39), which is consistent with [35, Eq. (4.4)]. Furthermore, all terms containing odd derivatives of the displacement field in (37) give a nonzero contribution only around the bridging region.
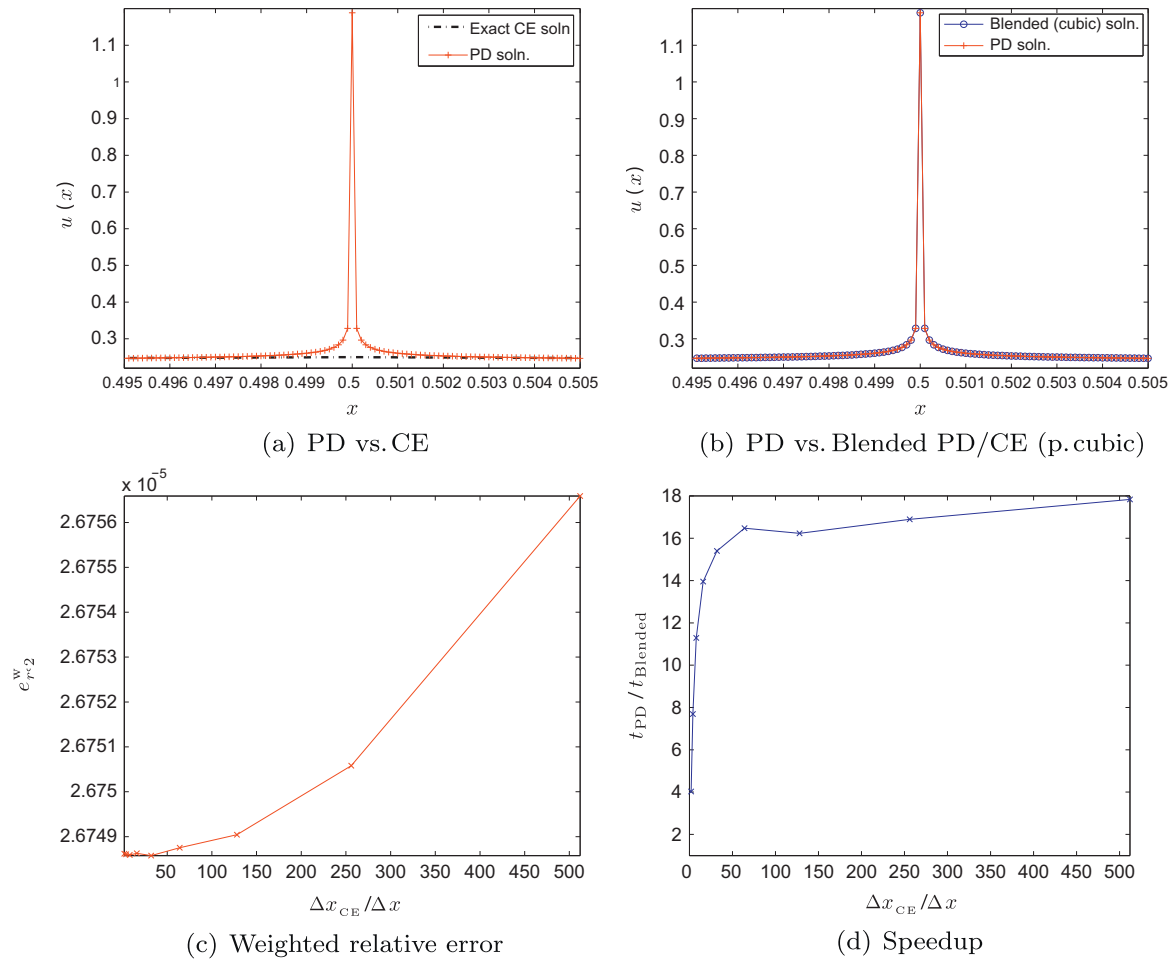
Fig. 14. (a) Comparison between the PD numerical solution and CE exact solution. (b) Comparison between the PD model solution and the blended PD/CE model solution (with cubic blending function), with $\Delta x_{CE} = 512 \times \Delta x$, (c) Weighted relative error (*cf.* (35)) as a function of the "pure" CE relative mesh size, and (d) time speedup as a function of the "pure" CE relative mesh size.

7. Summary and future work

In this paper, a consistent blending method to couple peridynamics and classical elasticity is presented. The novel result is that, in contrast to classical blending methods where two or more models are joined together, we derive a coupled nonlocal/local scheme from a single framework, in this case the nonlocal continuum peridynamics theory. By inserting blending functions in the nonlocal equation of motion in a symmetric way, we ensure that the nonlocal model satisfies the linear admissibility condition, for which Newton's third law holds. Furthermore, the methodology used to derived the coupled model ensures that the resulting blended model is patch test consistent, avoiding spurious undesired ghost forces; this is also demonstrated numerically. At the end of this paper, the proposed blended model is generalized to the coupling of peridynamics and higher-order gradient models of any order.

In contrast to most classical blending approaches for atomistic-to-continuum coupling, the blending weights are introduced here in a *nonlocal manner*, i.e., they are based upon integrals of blending functions; as a consequence, the classical bridging domain is extended to a *transition region* with size dependent on the length scale of the nonlocal model. In addition, our method works for a very general class of blending functions of the form of (9).

We have demonstrated numerically the accuracy and efficiency of the blended model in relation to a fully nonlocal model, and showed that the error can be controlled by the sizes of the nonlocal

region and the transition region; very small errors can be achieved (see, e.g., Fig. 10). A qualitative study regarding modeling error was performed by studying the sensitivity of the blended model with respect to the location of a point load, showing the efficacy of the model as long as the point load is located inside the nonlocal domain far enough from the transition regions. We also performed initial studies concerning the speedup obtained in the blended model with respect to the fully nonlocal model, showing a significant reduction in the computational time.

Generalizations to nonlinear models in higher dimensions and applications to material damage situations for which peridynamics is advantageous, will be pursued in a future publication. Furthermore, we plan to extend the current work to provide analytical quantifications of some of the numerics presented here, as well as develop and implement adaptive algorithms to control the modeling error.

Acknowledgements

References

[1] B. Alali, Multiscale Analysis of Heterogeneous Media for Local and Nonlocal Continuum Theories, Ph.D Thesis, Louisiana State University, 2008.

[2] E. Askari, F. Bobaru, R.B. Lehoucq, M.L. Parks, S.A. Silling, O. Weckner, Peridynamics for multiscale materials modeling, in SciDAC 2008, 13–17 July, Washington, J. Phys.: Conf. Ser., vol. 125, 2008, p. 012078.

[3] S. Badia, P. Bochev, R. Lehoucq, M. Parks, J. Fish, M. Nuggehally, M. Gunzburger, Int. J. Multiscale Comput. Eng. 5 (2007) 387–406.

[4] S. Badia, M. Parks, P. Bochev, M. Gunzburger, R. Lehoucq, Multiscale Model. Simul. 7 (2008) 381–406.

[5] P.T. Bauman, H.B. Dhia, N. Elkhodja, J.T. Oden, S. Prudhomme, Comput. Mech. 42 (2008) 511–530.

[6] P.T. Bauman, J.T. Oden, S. Prudhomme, Comput. Methods Appl. Mech. Eng. 198 (2009) 799–818.

[7] T. Belytschko, S.P. Xiao, Int. J. Multiscale Comput. Eng. 1 (2003) 115–126.

[8] H. Ben Dhia, C.R. Acad. Sci. Paris, Série IIb 326 (1998) 899–904.

[9] H. Ben Dhia, Numerical modeling of multiscale problems: the Arlequin method, in: W. Wunderlich (Ed.), Proceedings of the First European Conference on Computational Mechanics, Muenchen, Germany, 1999.

[10] F. Bobaru, M. Duangpanya, Int. J. Heat Mass Transfer 53 (2010) 4047–4059.

[11] F. Bobaru, Y.D. Ha, Int. J. Multiscale Comput. Eng. 9 (2011) 635–660.

[12] F. Bobaru, M. Yang, L.F. Alves, S.A. Silling, E. Askari, J. Xu, Int. J. Numer. Methods Eng. 77 (2009) 852–877.

[13] P. Bochev, R. Lehoucq, M. Parks, S. Badia, M. Gunzburger, in: J. Fish (Ed.), Multiscale Methods: Bridging the Scales in Science and Engineering, Oxford University Press, Oxford, 2009, pp. 165–189 (Chapter 6).

[14] W.A. Curtin, R.E. Miller, Modell. Simul. Mater. Sci. Eng. 11 (2003) R33–R68.

[15] E. Emmrich, O. Weckner, Math. Model. Anal. 12 (2007) 17–27.

[16] J. Fish, M.A. Nuggehally, M.S. Shephard, C.R. Picu, S. Badia, M.L. Parks, M. Gunzburger, Comput. Methods Appl. Mech. Eng. 196 (2007) 4548–4560.

[17] J.T. Foster, S.A. Silling, W.W. Chen, Int. J. Numer. Methods Eng. 81 (2010) 1242–1258.

[18] Y.D. Ha, F. Bobaru, Int. J. Fract. 162 (2010) 229–244.

[19] F. Han, G. Lubineau, Int. J. Numer. Methods Eng. 89 (2012) 671–685.

[20] B. Kilic, E. Madenci, J. Mech. Mater. Struct. 5 (2010) 707–733.

[21] J. Knap, M. Ortiz, J. Mech. Phys. Solids 49 (2001) 1899–1923.

[22] B.V. Koten, M. Luskin, SIAM J. Numer. Anal. 49 (2011) 2182–2209.

[23] E. Kröner, Int. J. Solids Struct. 3 (1967) 731–742.

[24] I.A. Kunin, Elastic Media with Microstructure I: One-Dimensional Models, Springer Series in Solid State Sciences, vol. 26, Springer-Verlag, Berlin, 1982.

[25] I.A. Kunin, Elastic Media with Microstructure II: Three-Dimensional Models, Springer Series in Solid State Sciences, vol. 44, Springer-Verlag, Berlin, 1983.

[26] G. Lubineau, Y. Azdoud, F. Han, C. Rey, A. Askari, J. Mech. Phys. Solids 60 (2012) 1088–1102.

[27] R.W. Macek, S.A. Silling, Finite Elements Anal. Des. 43 (2007) 1169–1178.

[28] R.E. Miller, E.B. Tadmor, Modell. Simul. Mater. Sci. Eng. 17 (2009) 053001.

[29] S. Prudhomme, H.B. Dhia, P.T. Bauman, N. Elkhodja, J.T. Oden, Comput. Methods Appl. Mech. Eng. 197 (2008) 3399–3409.

[30] D. Rogula, Introduction to Nonlocal Theory of Material Media, in: D. Rogula (Ed.), Nonlocal Theory of Material Media, Springer-Verlag, Berlin, 1982, pp. 125–222.

[31] P. Seleson, Peridynamic Multiscale Models for the Mechanics of Materials: Constitutive Relations, Upscaling from Atomistic Systems, and Interface Problems, PhD thesis, Florida State University, 2010.

[32] P. Seleson, M. Gunzburger, Commun. Comput. Phys. 7 (2010) 831–876.

[33] P. Seleson, M.L. Parks, Int. J. Multiscale Comput. Eng. 9 (2011) 689–706.

[34] P. Seleson, M.L. Parks, M. Gunzburger, Peridynamic solid mechanics and the embedded-atom model (submitted for publication).

[35] P. Seleson, M.L. Parks, M. Gunzburger, R.B. Lehoucq, Multiscale Model. Simul. 8 (2009) 204–227.

[36] V.B. Shenoy, R. Miller, E.B. Tadmor, R. Phillips, M. Ortiz, Phys. Rev. Lett. 80 (1998) 742–745.

[37] S.A. Silling, J. Mech. Phys. Solids 48 (2000) 175–209.

[38] S.A. Silling, E. Askari, Comput. Struct. 83 (2005) 1526–1535.

[39] S.A. Silling, M. Epton, O. Weckner, J. Xu, E. Askari, J. Elasticity 88 (2007) 151–184.

[40] S.A. Silling, R.B. Lehoucq, J. Elasticity 93 (2008) 13–37.

[41] E.B. Tadmor, M. Ortiz, R. Phillips, Philos. Mag. A 73 (1996) 1529–1563.

[42] S.P. Xiao, T. Belytschko, Comput. Methods Appl. Mech. Eng. 193 (2004) 1645–1669.